USING STORM KINEMATICS AND SURFACE OZONE MEASUREMENTS TO DESCRIBE THE CONVECTIVE TRANSPORT IN DOWNDRAFTS OVER THE BRAZILIAN AMAZON

A Thesis

by

HANNAH MARIE UPTON

Submitted to the Office of Graduate and Professional Studies of
Texas A&M University
in partial fulfillment of the requirements for the degree of

MASTER OF SCIENCE

Chair of Committee,	Courtney Schumacher
Co-Chair of Committee,	R. Saravanan
Committee Member,	David Sparks
Head of Department,	Ping Yang

December 2016

Major Subject: Atmospheric Sciences

ABSTRACT

A correlation between enhancements in surface ozone observations and decreased equivalent potential temperature (i.e. surface downdraft identifiers) is observed in the Brazilian Amazon during convective events. Meteorological and chemical data collected during the Green Ocean Amazon (GoAmazon 2014/5) field campaign are used to explore the link between storm kinematics and surface ozone enhancement events. Contoured frequency by altitude diagrams (CFADs) of S-band radar reflectivity values are used to gather more information about the structure and evolution of storms during ozone enhancement events in the Amazon. Using a smaller domain than previous CFAD studies, the evolution of individual storm characteristics (i.e. downdrafts) is more apparent. A branch of higher reflectivity breaking off near 7 km and descending to the surface is observed in the CFADs near the time of descending motion and maximum surface ozone. This phenomenon, which we refer to as a descending arm, is found to be a robust feature during ozone events.

Case studies of varying surface ozone enhancement intensities illustrate the relationship between the shape and distinctiveness of the descending arm and the timing and magnitude of the enhancement events. Strong ozone enhancements correspond to stronger, well-defined descending arms. Vertical velocity retrievals from vertical profilers are used to confirm the presence of descending motion. A descending arm metric is created to automate the detection of descending arms and their relative strength. Future work will refine this metric and allow us to test the sensitivity of

descending arms on other environmental factors and their use in identifying convective cold pools.

TABLE OF CONTENTS

Page

LIST OF FIGURES

Page

1. INTRODUCTION

1.1 Convective Structure and Lifecycle

Atmospheric convection starts with a parcel of warm, moist air that finds itself less dense than the surrounding air and begins to rise. This is known as the cumulus stage of a convective cell's lifecycle and is marked by an increasing rate of ascent as the parcel cools, water condenses, and latent heat is released, which enhances the temperature difference between the cell and the environment. The storm transitions to a mature stage when a downdraft is initiated by precipitation with fall speeds greater than the updraft can support. This stage is marked by the onset of rain and the presence of free-tropospheric air at the surface. This cool, near saturated air descends rapidly in a convective downdraft from near the ambient cloud layer at 800-900 mb or higher up within the cumulonimbus (Zipser 1977).

The final, dissipating stage of a convective cell occurs when the downdraft cuts off the source of warm moist air to the storm. The schematic in Figure 1 illustrates the life cycle of a single convective cell. In the presence of vertical wind shear or through the aid of certain storm characteristics (e.g., gust fronts) multiple cells can develop and feed off of one another during the mature stage.

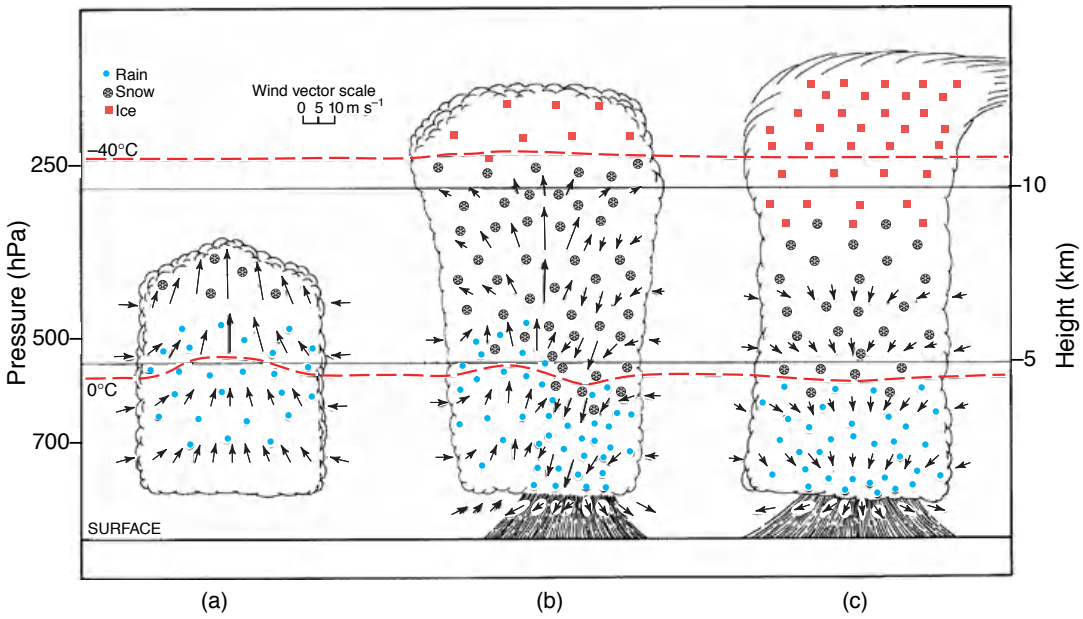

Figure 1. The evolution of a single convective cell. From Wallace and Hobbs (2006).

1.2 Convective Transport (Up and Down)

At the beginning and end of this process there is convective transport of air between the lower troposphere and the upper troposphere in both directions (Zipser 1969,1977). This redistribution of air is the link between deep convection and the sources and sinks of trace gases such as ozone (Garstang et al. 1988, Figure 2). Tracking the distribution of these gases in the presence of convection requires an understanding of storm evolution, draft structures and parcel trajectories (Scala et al. 1990).

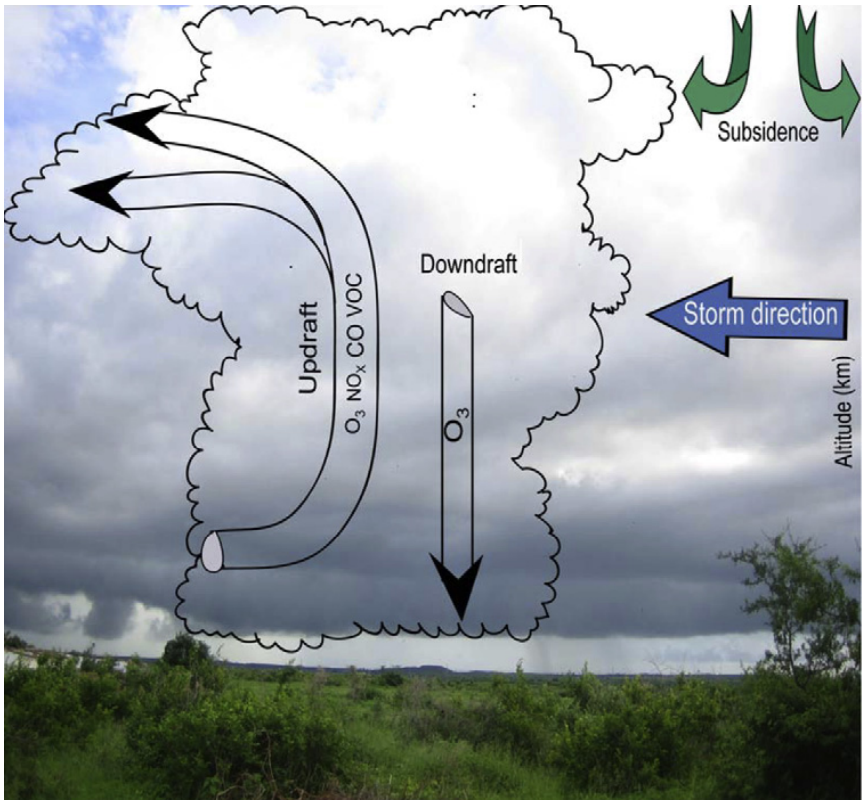

Figure 2. A schematic showing the transport of ozone and ozone precursors in convective up and down drafts and in the trailing stratiform region during a convective event. Image adapted from Grant et al. (2008).

Chatfield and Crutzen (1984) hypothesized deep convection to be a major redistributor of trace gases from the boundary layer to the free troposphere, which was later supported by observational evidence in Dickerson et al. (1987). These studies and many others, including Gidel (1983) and Greenhut (1986), all note the important influence of convection on the vertical distribution of trace gases.

Most of this previous work is focused on the transport of air upwards via convective updrafts and the implications for the chemistry of the upper troposphere

(Bertram et al. 2007). Particularly in the Brazilian Amazon much work has been done to characterize the transport of biomass burning products (Pickering et al. 1996) and ozone (Garstang et al. 1988, Kirchoff et al. 1996) from the surface.

Not as well documented is the contribution of convective downdrafts, despite the fact that the magnitude of this transport can be similar or greater than the updraft portion and can balance the upward transport (Garstang et al. 1988, Grant et al. 2008). A handful of studies (Betts et al. 2002, Grant et al. 2008, Gerken et al. 2015) have considered the transport of ozone rich air from the mid troposphere (where tropospheric ozone in the tropics typically maximizes) down to the surface during the mature stage of a convective cell. The magnitude of these ozone enhancement events depends on the vertical distribution of ozone and the origin of the downdraft (Gerken et al. 2015). The majority of the previous studies are chemistry oriented and the downdraft origin and transport processes behind this transport are not well understood.

Grant et al. (2008) were the first to use tower-based instruments, ozonesondes, and radar to study the influence of convective downdrafts on surface ozone enhancements in western Senegal. Similar increases in surface ozone during convective events were observed in the Bay of Bengal (Sahu and Lal 2006) and in the Amazon (Betts et al. 2002).

Environmental factors including storm characteristics, time of day, and seasonality can impact the magnitude of surface ozone events. The strength of convective velocities and the height origin of the downdraft impact the amount surface ozone is enhanced during convective events. Convective velocities greater than 10 m/s

are sufficient for the transport of ozone to the surface (Grant et al. 2008), but stronger velocities don't always lead to greater enhancements. Stronger storms can transport air with increased levels of ozone from higher levels increasing the surface ozone levels (Grant et al. 2008). Conversely, stronger storms can lead to more mixing which reduces the vertical ozone gradient and can lead to smaller increases in ozone at the surface (Gerken et al. 2015). There is a diurnal component as well; intense ozone events can occur at night because there is a stronger gradient between the boundary layer and tropospheric ozone due to higher rates of dry deposition at night and better mixed conditions during the day (Betts et al. 2002, Gerken et al. 2015). The rainy season typically sees smaller values of ozone at the surface due to reduced precursors such as NOx and biomass burning products, reduced radiance due to increased cloudiness, and increased surface deposition with higher amounts of surface vegetation. This increases the vertical gradient of ozone and can lead to stronger events in the rainy season (i.e., February-April) (Betts et al. 2002). Stratiform regions of convective storms can also efficiently transport ozone to the boundary layer in lower concentrations over longer time scales (Lelieveld and Crutzen 1994).

1.3 Ozone

The redistribution of ozone in the troposphere influences atmospheric chemistry cycles and Earth's surface energy budget. Transport of ozone to the surface by convective downdrafts reduces its lifetime because of the increased sinks (Grant et al. 2008). Downdraft transported ozone increases levels of HO and subsequent reactions

can change the oxidation capacity of the lower atmosphere. These reactions decrease the greenhouse effect by reducing the amount of methane and carbon monoxide at the surface (Grant et al. 2008). The presence of ozone also keeps gases such as CO and NOx below harmful levels (Betts et al. 2002). Ozone is a strong absorber of thermal energy in the atmospheric window, so increased concentrations can alter the surface energy budget (Betts et al. 2002). Enough ozone is transported by downdrafts to influence the local chemistry of the Amazon and decrease the levels of natural rainforest emitted hydrocarbons (Gerken et al. 2015).

Ozone values monotonically increase with height in the tropical troposphere (Kirchoff et al. 1990, Gerken et al. 2015). Over the Amazon, ozone values increase at an average rate of 6 ppbv/km in the wet season (Grant et al. 2008). Figure 3 shows an average vertical profile of ozone in Manaus for both the wet and dry seasons. Ozone profiles follow the lead of the surface, as can be seen by the decrease in ozone toward the surface during the wet season through the whole troposphere (Kirchoff et al. 1996). An average ozone profile increases with height in the lowest 3-5 km and then remains steady above 5-6 km until the influence of stratospheric ozone leads to a steady increase with height above 10 km.

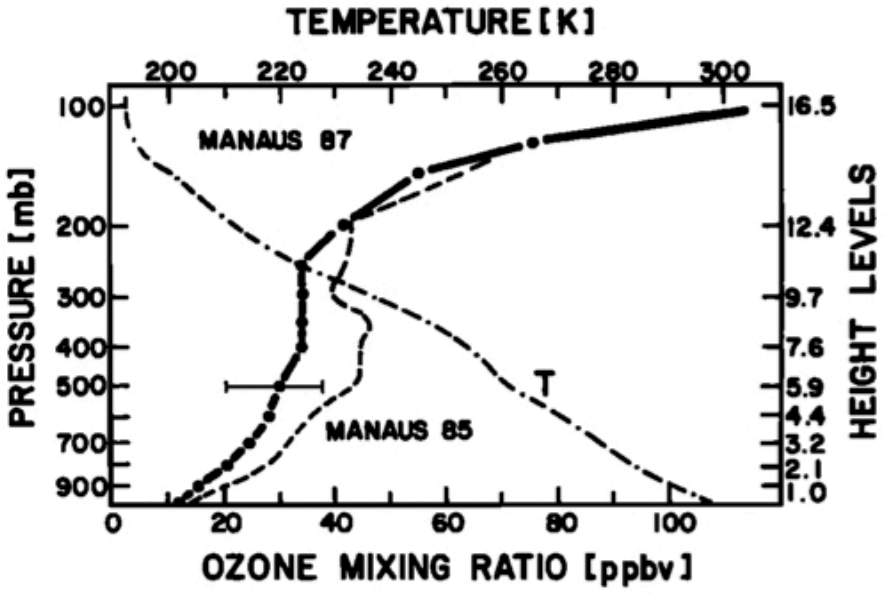

Figure 3. An average wet season (thick dash-dot line) and dry season (dashed line) vertical ozone profile for the year 1987. The average temperature profile (thin dash-dot line) is also shown. Image adapted from Kirchoff et al. (1990).

There are several sources of ozone above the boundary layer including reactions with the abundant NOx from frequent lightening in the tropical mid to upper troposphere (Dickerson et al. 1987, Pickering et al. 1996, Bertram et al. 2007) and some transport from the lower stratosphere (Kirchoff et al. 1990, Thompson et al. 1997). Ozone behavior at the surface is more complex. Ozone sinks at the surface include surface deposition and reactions with NO, CO, and hydrocarbons (Grant et al. 2008). During the wet season the increased vegetation increases the amount of ozone lost at the surface leading to smaller surface values and a stronger gradient with height (Betts et al. 2002). Photochemical and catalytic reactions near the surface produce and destroy ozone. Ozone values at the surface are greater during the dry season due to less deposition with

reduced vegetation and decreased cloudiness leading to more photochemical production. Surface values of ozone have an average diurnal peak of 12 ppbv in the dry season and 6 ppbv in the wet season near Manaus, Brazil, which is significantly lower than other locations at similar latitudes, because of the increased vegetation. Forested regions have even smaller surface ozone concentrations (Kirchoff et al. 1990). Factors influencing surface ozone values include timing and proximity of precipitation and biomass burning events. Drier sites tend to have higher concentrations of ozone, but the effect of rain doesn't seem to depend on the amount of precipitation observed (Kirchoff et al. 1996).

Convection plays a role in the distribution of ozone vertically and in the amount at the surface. During convective events the presence of lightning leads to increased levels of NOx, a precursor for ozone production. Convection also mixes the troposphere, which decreases the vertical gradient of ozone. As discussed in Section 1.2 convective up and down drafts displace ozone at or to the surface. The increases from convective transport by downdrafts typically last 1-2 hours.

Figure 4 shows the mean diurnal profile of ozone at the surface during the month of February. The magnitude of the cycle shifts seasonally, but the pattern is consistent. (Betts et al. 2002). Surface ozone values are at a maximum during the day when vertical mixing is strongest, which transports ozone from aloft down to the surface. Local photochemical processes are also most active at this time of day. Ozone peaks around noon. As the surface cools off at night, the boundary layer becomes decoupled eliminating entrainment of ozone and after sunset there is no longer photochemical sources. Ozone is destroyed at night by reactions with NO, produced by soils, and

deposition at the surface. Ozone reaches it's lowest value at night, which can be nearly zero in forested regions (Grant et al. 2008).

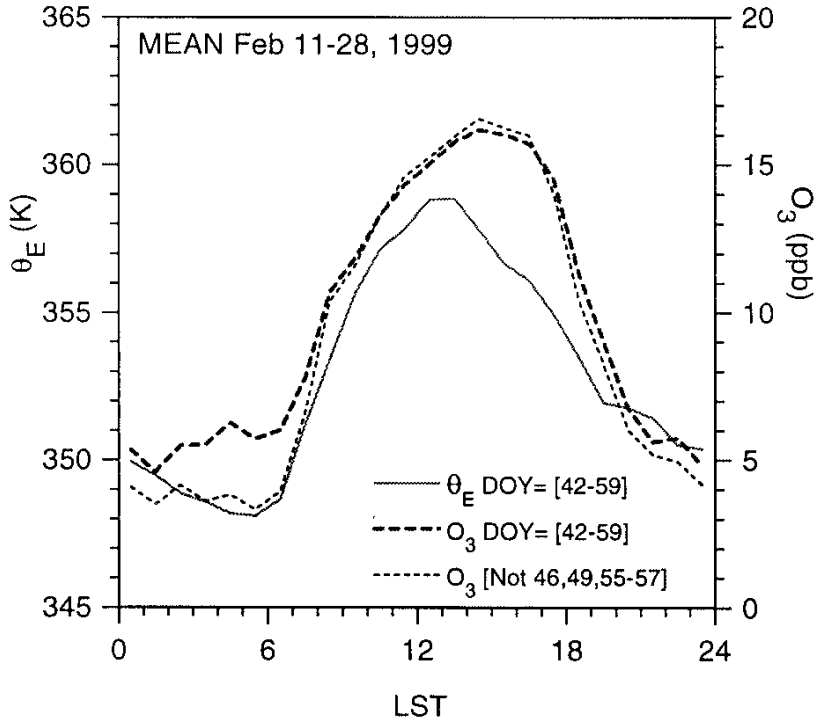

Figure 4. The mean diurnal cycle of theta-e and ozone at the surface from February 11-28, 1999. Image adapted from Betts et al. (2002).

1.4 Theta-e Profiles

It is useful to know approximately where in the atmosphere the parcel of air observed during an ozone event came from and if it descended rapidly in a convective downdraft. A useful quantity that can be calculated with readily available observations is equivalent potential temperature, often referred to as theta-e. Theta-e makes a good tracer because it is conserved in evaporation and condensation processes (Emanuel

1994). Decreases in surface theta-e values are evident in all identified surface ozone events for our study. Changes in theta-e vary from 2.55 to 20.33 K and often occur simultaneously with the increase in ozone. Previous studies that have used theta-e to track downdraft air include Zipser (1969), Betts (1973), and Betts and Silva Dias (1979); see also Figure 5.

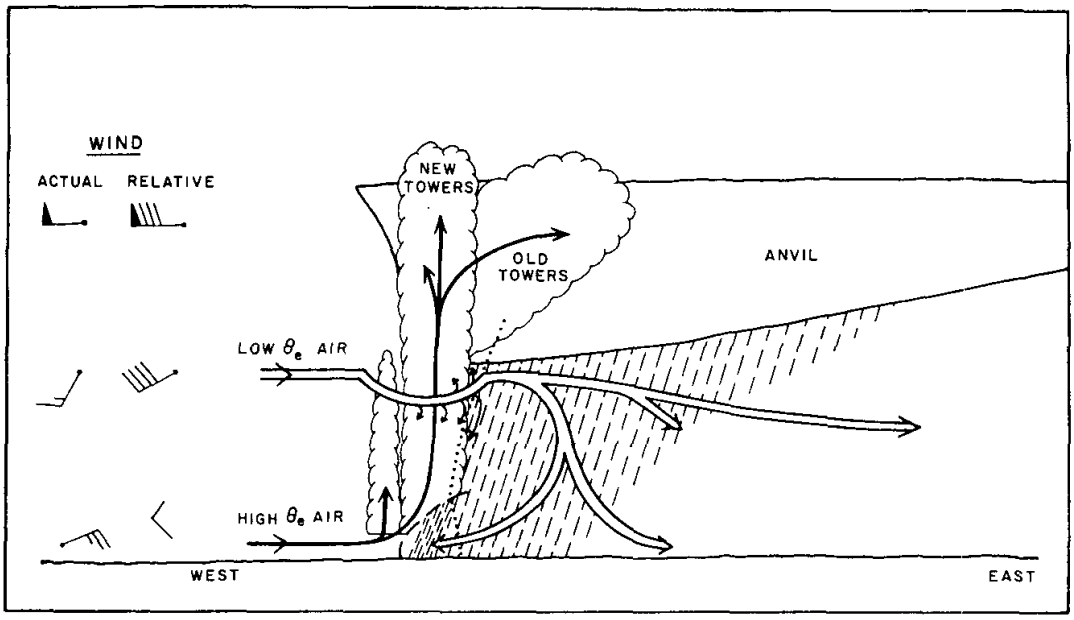

Figure 5. A schematic showing potential pathways of air with lower theta-e values down to levels with higher ambient theta-e values during a convective event. From Zipser (1969).

Theta-e is calculated using observed air temperature (T), water vapor mixing ratio (r), and barometric pressure (p), all of which are readily available from soundings and meteorological measurements made at our instrument site. The remaining constants

are the latent heat of vaporization (Lv), the dry heat capacity of air (cpd), the gas constant of dry air (Rd) and a reference pressure (p_0) of 1000hPa.

$$\theta_e \approx \left(T + \frac{L_v}{c_{pd}} r\right) \left(\frac{p_0}{p}\right)^{\frac{R_d}{c_{pd}}}$$

Unlike ozone, theta-e decreases with height in the tropical troposphere. The largest values of theta-e are at the surface because of the presence of surface and latent heat fluxes driven by solar heating. The main sink of theta-e is radiative cooling (Betts 1992). Within a convective downdraft, entrainment and evaporation of rain doesn't change the theta-e value. As this cool air sinks, the corresponding theta-e values, lower than the original surface air, confirm the presence of descending motion.

Figure 4 shows the mean diurnal cycle of theta-e at the surface during February 1999. Similar to ozone in the tropical troposphere reaches a minimum right before sunrise because the surface continuously cools throughout the night. Once the sun rises, theta-e increases rapidly to a peak near 360 K just after local noon. Theta-e decreases in the afternoon in the presence of convective downdrafts that bring down air with lower values of theta-e.

1.5 Objective

The object of this thesis is to unite storm kinematics and chemistry observations to describe the transport of ozone in convective downdrafts over the Brazilian Amazon. Using 3-D reflectivity data collected during the Green Ocean Amazon

(GoAmazon2014/5) field campaign, I use a novel method to illustrate the downward transport of air in a convective system and to detect and describe the height and magnitude of convective downdrafts and their associated ozone transport over the Amazon.

2. DATA AND METHODS

2.1 GoAmazon2014/5

The Observations and Modeling of the Green Ocean Amazon (GoAmazon) experiment took place in the Brazilian Amazon during 2014 and 2015 and collected meteorological and chemistry observations to better understand the influence of a pollution plume from the industrial city of Manaus, Brazil on local storm kinematics and chemistry. Figure 6 shows the location of Manaus and several surrounding instrument sites. The main instrument site, T3, was located ~70 km west of Manaus just outside the city of Manacapuru to intersect the pollution plume as many days as possible. A second site, ZF2, was located 60 km NNW of Manaus and was a source of clean, background observations.

Chemistry and meteorological observations were taken at these sites over the course of two years, particularly during two intensive operation periods (IOPs). The first IOP (IOP1) took place February-March 2014 and the second IOP (IOP2) took place August-September 2014. Relevant instrumentation for this study includes an S-band radar in Manaus, vertical wind profilers and an X-band radar at T3, and surface ozone observations at T3 and ZF2. These observations provide groundwork to further explore the convective transport of air to the surface during strong convective events.

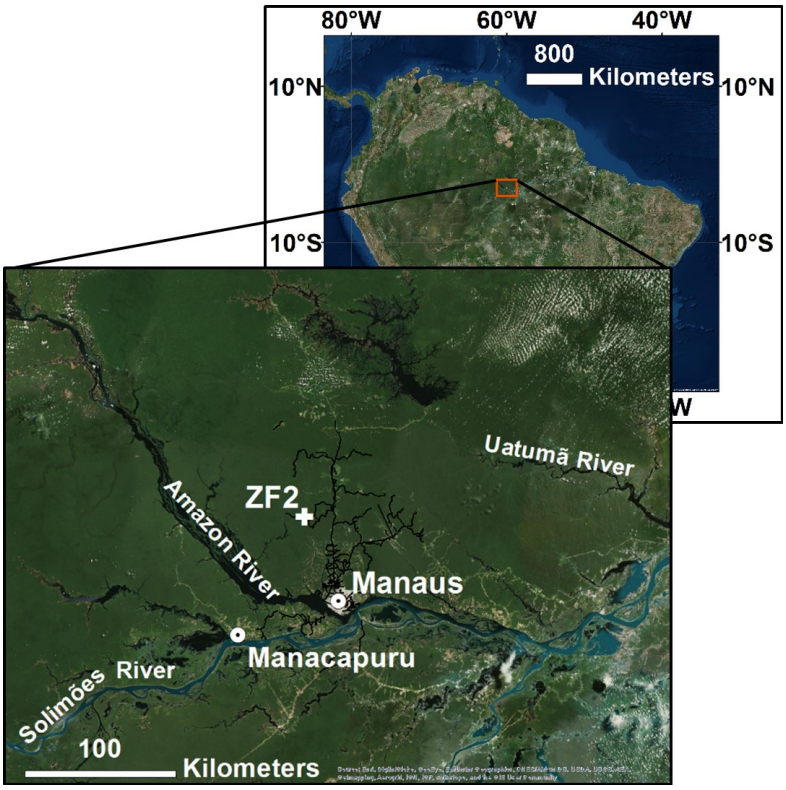

Figure 6. A map of South America showing the location of instrument sites for the GoAmazon2014/5 field campaign. Image adapted from Gerken et al. (2015).

2.2 SIPAM Radar

The Sistema de Proteção da Amazônia (SIPAM) S-band, Doppler radar located at the Manaus-AM airport (03°08’56’’S, 59°59’29’’W, elevation 102.4 m) provided consistent three-dimensional reflectivity measurements during the campaign. The Manaus radar is part of a network of S-band (10-cm wavelength), Doppler radars that operate across the Amazon. The radar operated a scan strategy with 17 elevation angles every 11 minutes with data recorded out to 250 km from the radar at 500 m resolution.

At this time we have access to SIPAM products from January 3, 2014 through August 17, 2015. Data was recorded out to 250 km, but is arguably only reliable out to 110 km because of the large beam width of the SIPAM radar. This range still allows a comfortable margin to observe storm evolution across the main instrument sites. The polar coordinate radar data is interpolated on a 2 km x 2 km grid.

The 17 elevation angles included in the scan strategy were: 0.9, 1.5, 2, 3, 4, 5, 6, 7, 8, 9, 10.5, 12, 13.5, 15, 16.5, 18, and 19° (Figure 7). The Internet connection in Manaus was inconsistent, so often the highest elevation angles, which were recorded last, are missing in the data set. Elevation angles at and below 13.5° are consistently available. The lack of higher elevation angles limited our ability to explore any echo top patterns relative to the ozone events.

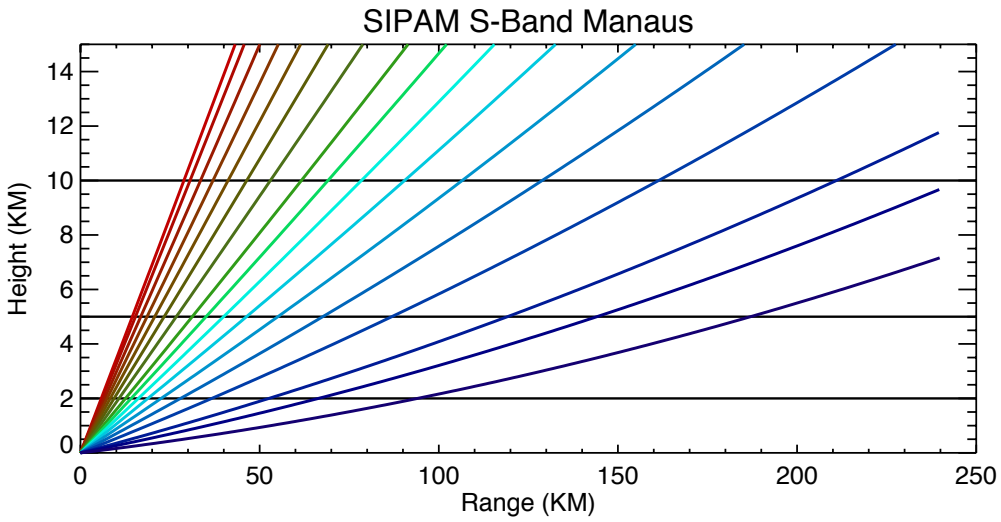

Figure 7. The 17 elevation angles used in the Manaus SIPAM radar scan strategy.

The SIPAM radar data was first calibrated using the TRMM PR ground validation technique described in Marks et al. (2009) and then monitored during the first three months of the campaign. An additional ground validation technique described in Silberstein et al. (2008) was used later on to fix abrupt discrepancies noticed in the radar returns. This technique uses stable ground clutter pixels located around the radar that should have stable returns day to day unless a change takes place to the radar system. Figure 8 shows the 95th percentile values of stable ground clutter pixels identified near the radar during 2014. Major changes seen in February and August 2014 imply a manual calibration shift was made. To compensate for these changes we added 2 dB to reflectivity values from February – 27 August 2014 and subtracted 3 dB to values from 28 August 2014 through September 2014.

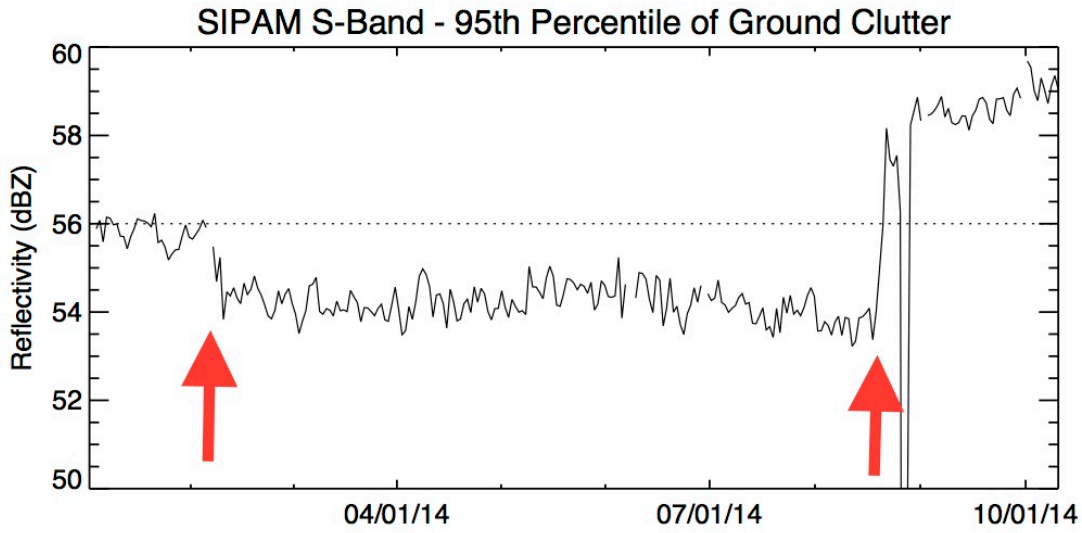

Figure 8. The 95th percentile value of ground clutter pixels near the SIPAM radar in Manaus, Brazil used to account for undocumented shifts in the radar system.

Reflectivity values can be correlated with rain gauges or drop size distributions (DSDs) from disdrometers to calculate rain rates over the radar domain. This relationship is known as a reflectivity-rain rate (Z-R) relationship and was first published by Marshall et al. (1948). A Josh-Waldvogel impact disdrometer operated by the Universidade do Estado do Amazonas (UEA) in Manacapuru was used to calculate a Z-R relationship for the first IOP (Feb/Mar 2014). The final Z-R relationship, $Z = 174.8 * R^{1.56}$ (Figure 9), was used to create monthly and seasonal rainmaps.

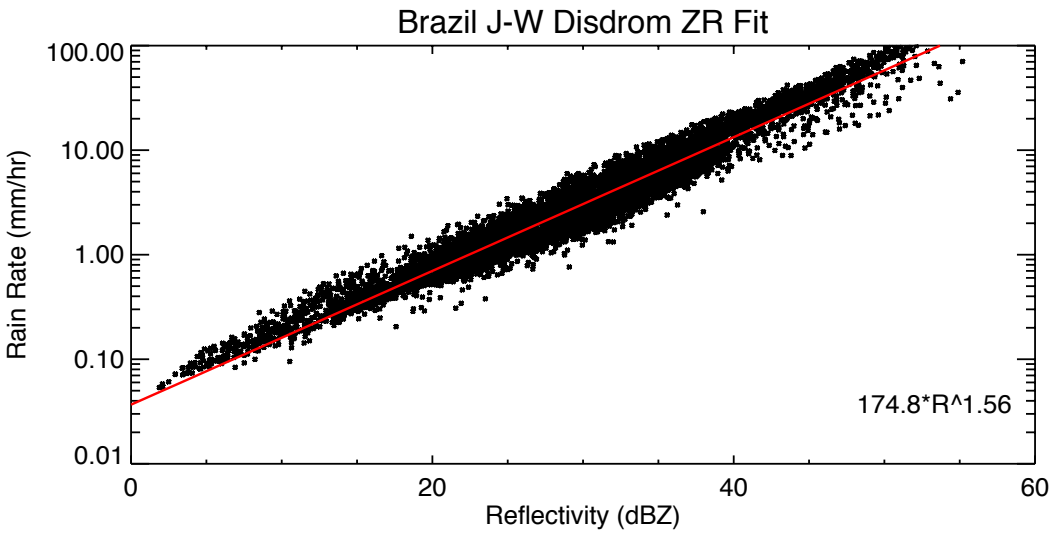

Figure 9. A Z-R relationship calculated for the 2014 wet season using SIPAM reflectivities and rain rates from a J-W disdrometer located at T3.

A CAPPI (constant altitude plan position indicator) image at 2.5 km was created for each 12 minute volume scan and then averaged together to create rainmaps for each IOP (Figure 10). A height of 2.5 km was found to be the most inclusive and

representative height for rain events in this region. Several regions of strong blockage are apparent in these images. For example, the NE corner of the radar domain and a slice directly south of the radar. These areas were removed using a mask before any statistics were calculated. Radar data is available out to 250 km but is most reliable within a radius of 110 km from the radar. The areas of the domain used for the majority of this study were free from any strong blockage or attenuation gaps.

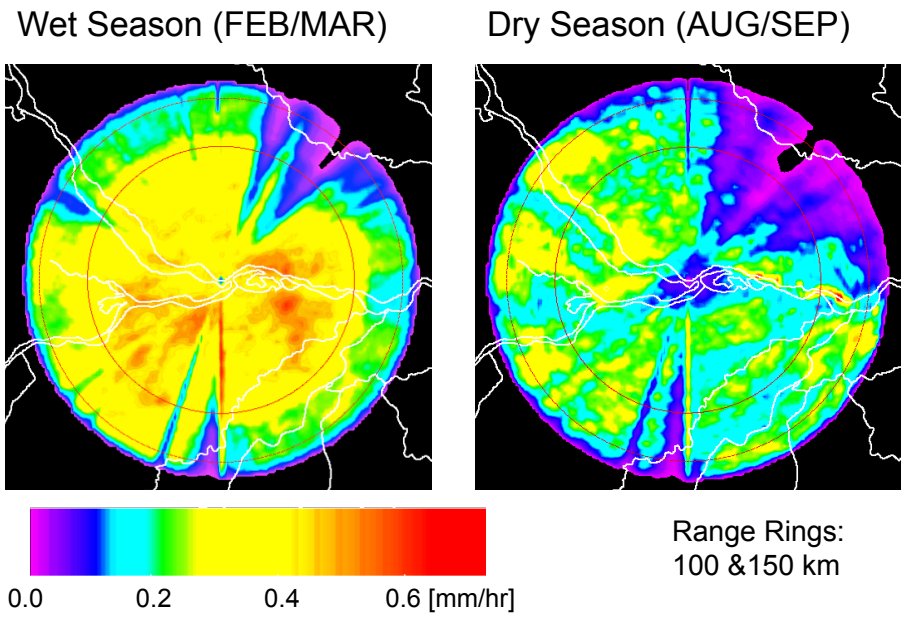

Figure 10. Average SIPAM radar rain maps centered on Manaus for the two IOPs. Rainrates shown in mm/hr based on 2.5 km CAPPIs. The inner red ring indicates a radius of 110 km and the outer 150 km from the SIPAM radar.

The climatology of the Amazon basin is split into three distinct seasons: wet, dry, and transition with maximum rainfall during the wet season in March and a minimum at the peak of the dry season in August (Machado et al. 2004). These well established

seasonal variations in Amazon rainfall can be seen in the rain maps created with SIPAM corrected reflectivity and the Z-R relationship mentioned above (Figure 11). February through May experience large, more organized systems with widespread stratiform rain, characteristic of the wet season. Convective cells during the dry season are smaller, but often more intense and are more influenced by local forcings such as the river/land breeze and the diurnal cycle. Convective cells during the dry season cover a much smaller area, but still account for a significant portion of annual rainfall across the basin.

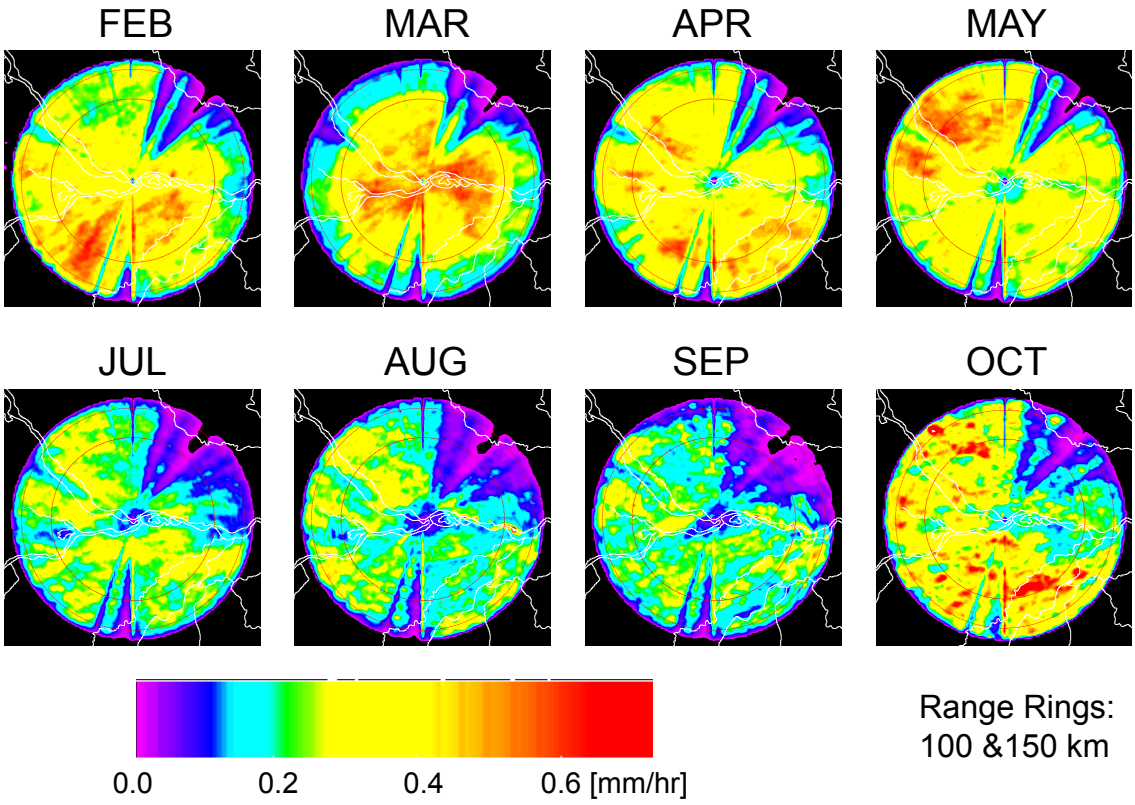

Figure 11. Monthly SIPAM radar rainmaps for 2014.

2.3 Vertical Profilers

A UHF ARM zenith radar (UAZR) and a W-band ARM cloud radar (WACR) were located at T3 and provided vertical velocity retrievals for the duration of the campaign. The UAZR is a reconfigured wind profiler that points vertically and can collect data from deep convective clouds. The original function of the ARM 915-MHz UHF wind-profiler system which has a 9° beam width and 33-cm wavelength was to estimate lower tropospheric horizontal winds from the surface up to 6-8 km. Over time the profilers were reconfigured to only point vertically and are referred to as UAZRs in this mode (Giangrande et al. 2013). The WACR is a zenith pointing Doppler radar most widely used to determine cloud bottoms and tops. WACR products include reflectivity, radial velocity, and spectral width.

A combination of both radar's products was used by Scott Giangrande to create profiles of vertical velocity, mean Doppler velocity, reflectivity, rain rates, and spectral width over T3 for the duration of the campaign. A quick look at the products most relevant to this study is shown in Figure 12. The vertical velocity retrievals indicate the direction and speed of air motion once the fall speed contribution of media within the radar volume is removed. Velocities are shown in m/s and positive/negative values indicate upward/downward motion. UAZR reflectivity products are dependent on the number and size of media intersected by the radar signals and are calibrated using surface disdrometers located at T3. These products are available up to 16 km above the surface at a time interval that varies between 5-10 seconds.

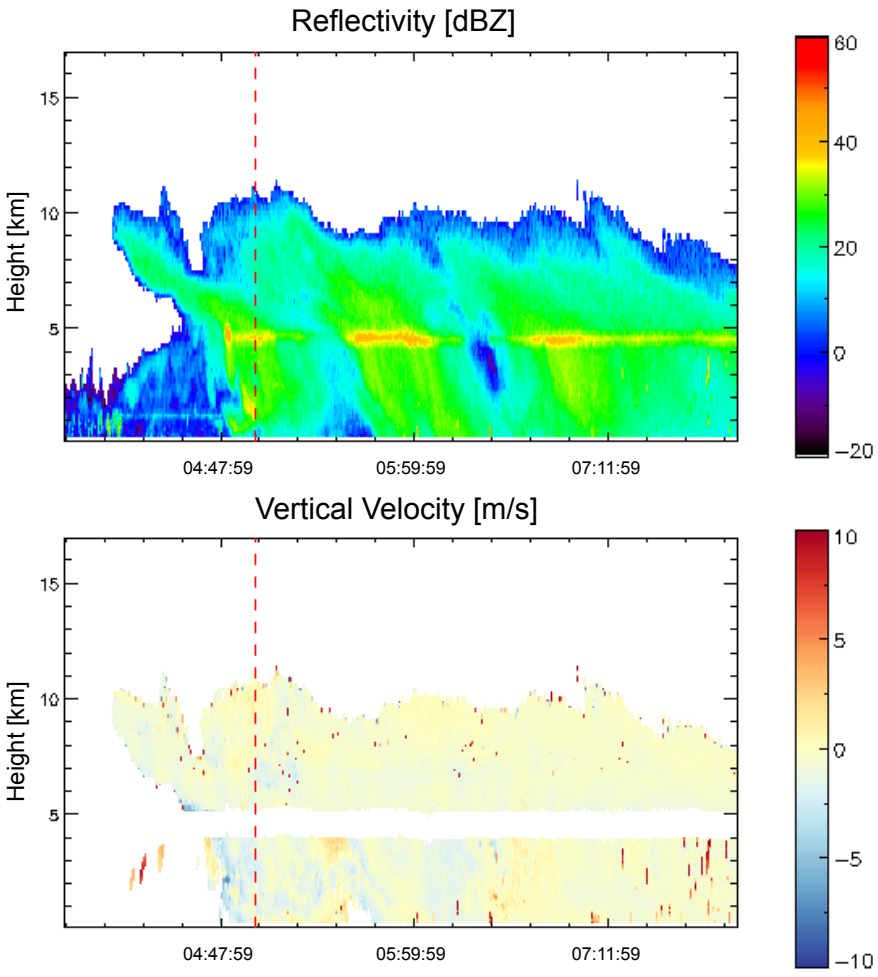

Figure 12. A quick look of the T3 vertical profiler products used in this study. These profiles are from 13 November 2014. In the bottom figure positive values indicate upward motion.

2.4 Ozone and Theta-e Measurements

Ozone observations were collected at both the ZF2 and T3 instrument sites using a model 49i, Thermo Fisher Scientific Inc. Surface (<100 m) ozone measurements were averaged into 5 and 30-minute values. Theta-e values were calculated from continuous temperature, relative humidity, and pressure measurements collected at T3.

Ozone enhancement events within the 5 minute averaged data was defined as an increase in ozone mixing ratio of at least 2.5 parts per billion by volume (ppbv) and a simultaneous decrease in theta-e of at least 2.5 K within a one hour time window. A total of 170 ozone events were observed at T3 from April 2014 to June 2015.

The magnitude of ozone enhancements ranged from 3.1 – 39.8 ppbv, with corresponding changes in theta-e from 2.5 – 20.3K. The distribution of ozone events throughout the year (Figure 13) roughly follows the precipitation climatology shown in Figure 11. There is an increase in events as you approach the wet season and a clear minimum in August when precipitation is at its lowest value of the year (Figure 13). There are exceptions, notably the month of February, which has much few events than expected. Figure 14 shows a distribution of ozone events by the magnitude of ozone change measured at the surface. Each bin represents ozone events within a 5 ppbv range, with starting points listed below the bars. The events are skewed toward smaller delta ozone values, with 89% of ozone enhancements below 18.1 ppbv and 73% below 13.1 ppbv.

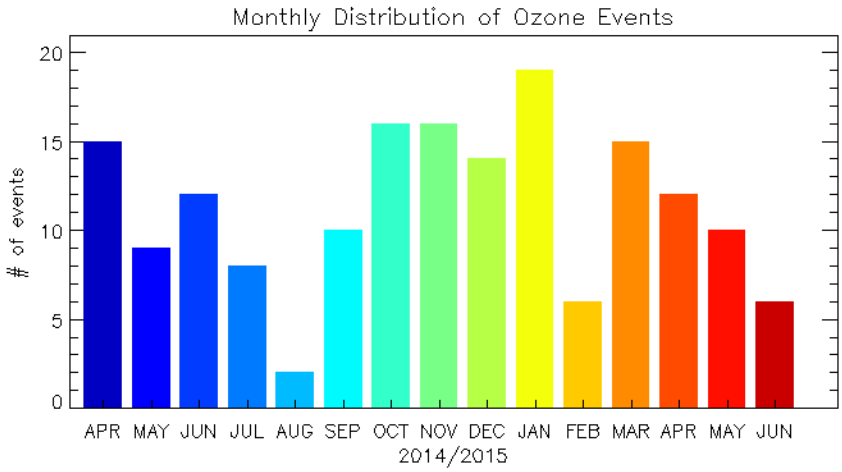

Figure 13. The monthly distribution of 170 ozone events observed at the T3 instrument site from April 2014 – Jun 2015.

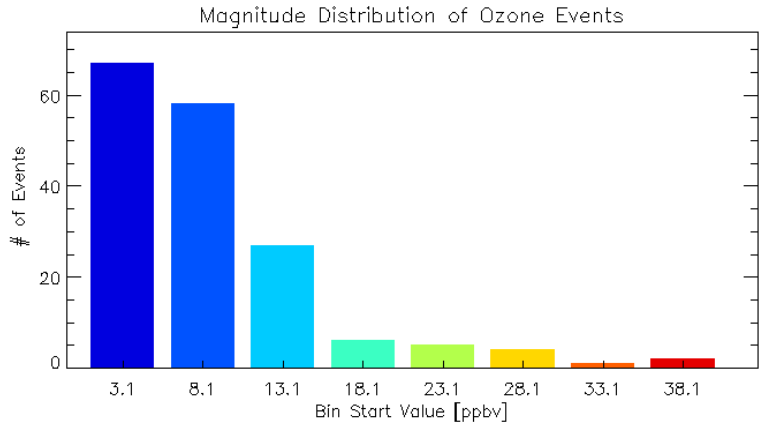

Figure 14. The 170 ozone events distributed by the magnitude of the ozone enhancement at the surface. Bin sizes are 5 ppbv. X-axis values represent the starting point for each bin.

2.5 CFAD Methodology

Contoured frequency by altitude diagrams (CFADs) of radar products (e.g. reflectivity, vertical velocities, and differential reflectivity) were first used to display

statistical distributions of storm properties by Yuter and Houze (1995). Compared to the typical cross section display of radar data, a CFAD illustrates the gross evolution of the storm (Figure 15). Cross sections suffer because of the narrow subset of data that can be viewed at one time. A CFAD gives a better representation of storm evolution across a domain instead of only at a single point in space.

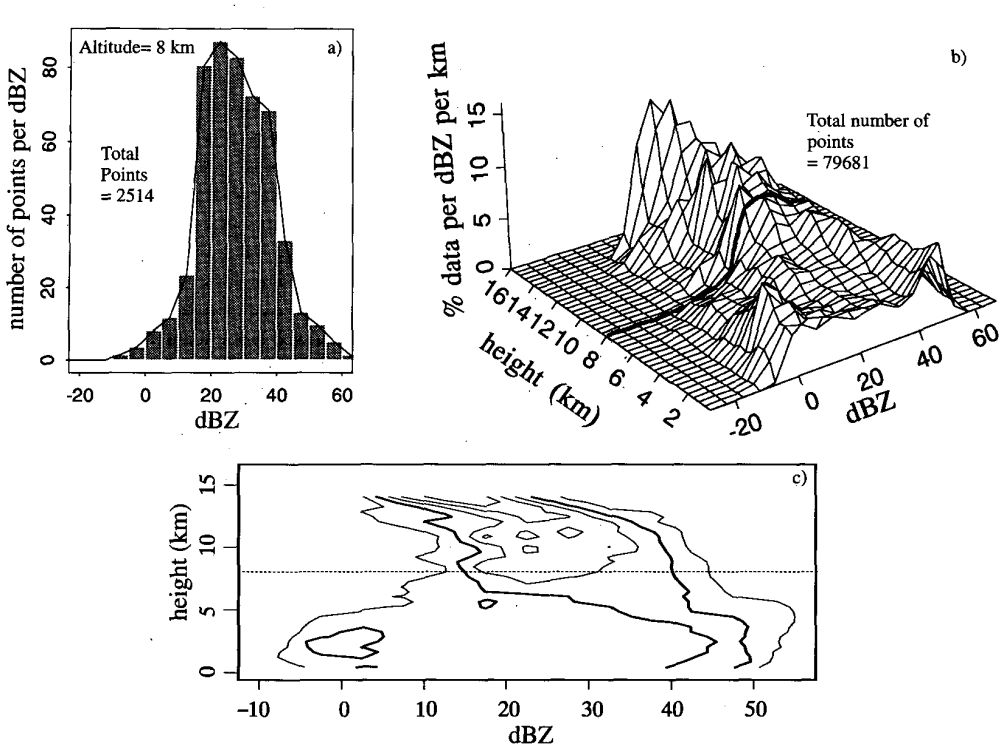

Figure 15. From Yuter and Houze (1995).

In a single plot, CFADs provide information about the frequency distributions of radar reflectivity values at every height level (in this study, 0.5-20 km every 0.5 km). At each height level, reflectivity values from 0-50 dBZ are binned with a bin size of 5 dB

and then normalized by the total number of points at that height level. The horizontal position of each grid cell is ignored. Contours of these normalized frequencies are then plotted in a coordinate system where the y-axis is height and the x-axis is reflectivity values (e.g., Fig. 15c). The contours are in units of percentage of point per unit variable per km and not percentage of data points. The labeled contour intervals used for the CFADs in this thesis are 0.1 0.2 0.3 0.4, and 0.5. The contour shading was done at higher resolution values of: 0.001, 0.005, 0.01, 0.02, 0.03, 0.04,0.05, 0.06, 0.08, 0.09, 0.1, 0.15, 0.2, 0.25, 0.3, 0.35, 0.4, 0.45, and 0.5. The individual contour levels were chosen to best illustrate the details in the frequency distributions. The contour patterns within the CFAD reveal information about the width and skewness of the frequency distributions at each level and the rate of change of these distributions with height within the same volume and from one volume to the next (Yuter and Houze 1995).

The main difference between my CFADs and those of Yuter and Houze (1995) is the size of my domain. Their original CFADs were made over a radar volume of 40 km x 39 km x 17.2 km, which is fairly small compared to most studies that composite CFADs over the entire radar grid. I experimented with smaller domain sizes to illuminate individual storm structures that are washed out in CFADs made across large grids. For this work, reflectivity below an altitude of 2 km was not included in the CFADs to avoid ambiguity due to ground clutter. A lower threshold was applied to the normalized frequencies so that any level that contributed less than 0.3% of the total counts was not included in the final image. This condition eliminated levels above 12-15

km for most cases, which were sparsely populated and skewed the distribution away from reality.

The reflectivity fields from all the volume scans available during the two IOP periods were composited to create seasonal CFADs (Figure 16). The composites were made using the 22 x 22 km box size CFADs. Normalized frequency distributions at every height level were averaged with that same height level for all the scans available for the particular composite category. The final product was a CFAD with each level representing the average frequency distribution at that height level over the time period.

The first IOP, which took place February and March of 2014, is representative of the wet season climatology. The second IOP took place in August and September of 2014 and is characteristic of the transition season climatology. Because of limitations due to the operational radar characteristics, reflectivity values < 10 dBZ were removed at all levels. The IOP1 CFAD shows a more narrow distribution of reflectivities at all heights and does not reach as high of values as IOP2 CFAD. The IOP2 CFAD is indicative of dry season convection, which is often stronger, as illustrated by the higher reflectivity values aloft.

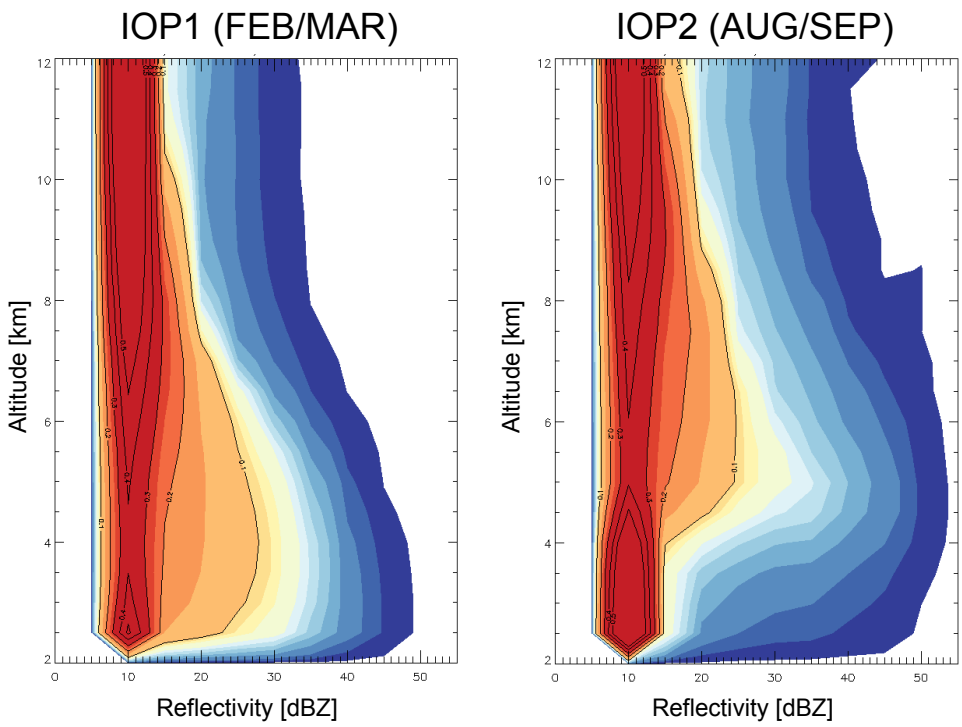

Figure 16. CFAD composites for each IOP. IOP1 is an average of February/March 2014 and IOP2 is an average of August/September 2014.

2.6 CFAD Application to Ozone Events

The CFADs created with the methodology described above can be used to gather more information about the structure and evolution of storms during ozone enhancement events in the Amazon. CFADs give a unique insight into the evolution of storms from convective to stratiform stages. CFADs from a 19 June 2014 system that passed over the ZF2 instrument site illustrate this transition very well (Fig. 17). The CAPPI image shows a leading line of convective cells followed by a widespread stratiform region.

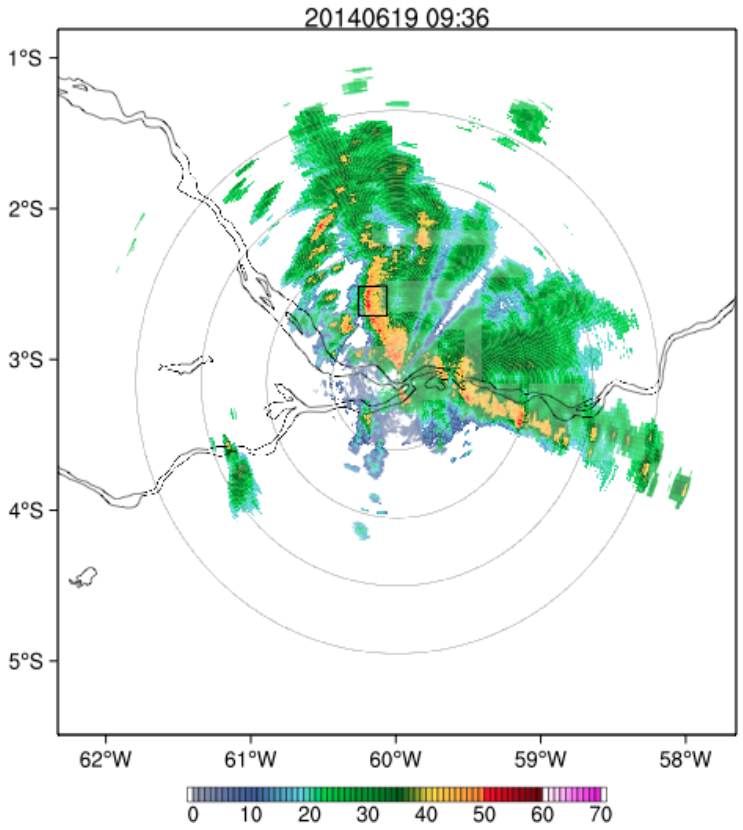

Figure 17. A CAPPI image showing the storm that passed over ZF2 on 19 June 2014. The black box north of Manaus represents the ZF2 instrument site.

Figure 18 is an idealized schematic of the lifetime of a convective cloud and its transition from convective to stratiform stages. In the beginning stages of a convective updraft air is being lofted where it can cool and condense. Reflectivity values at this stage are small as droplets are still growing. Eventually the hydrometeors reach a size that the updraft cannot support and descending motion begins to collapse the updraft. Precipitation laden downdrafts continue to reach the surface as the storms transitions to a stratiform profile with an extended anvil at upper levels. Figure 19 illustrates this same

transition in radar reflectivity values in a time height space. In the updraft portion at the beginning of the storm reflectivity values increase from left to right as the updrafts gain strength and hydrometeors grow. Around 1818 GMT the highest surface reflectivity values are observed. Reflectivity values are high for the entire vertical extent at this time. This represents the downdraft initiation and the onset of strong, sudden precipitation at the surface. As the storm transitions to a stratiform stage higher reflectivity values are observed at lower levels where it is raining and lower values (10 – 30 dBZ) are observed in the extended anvil area.

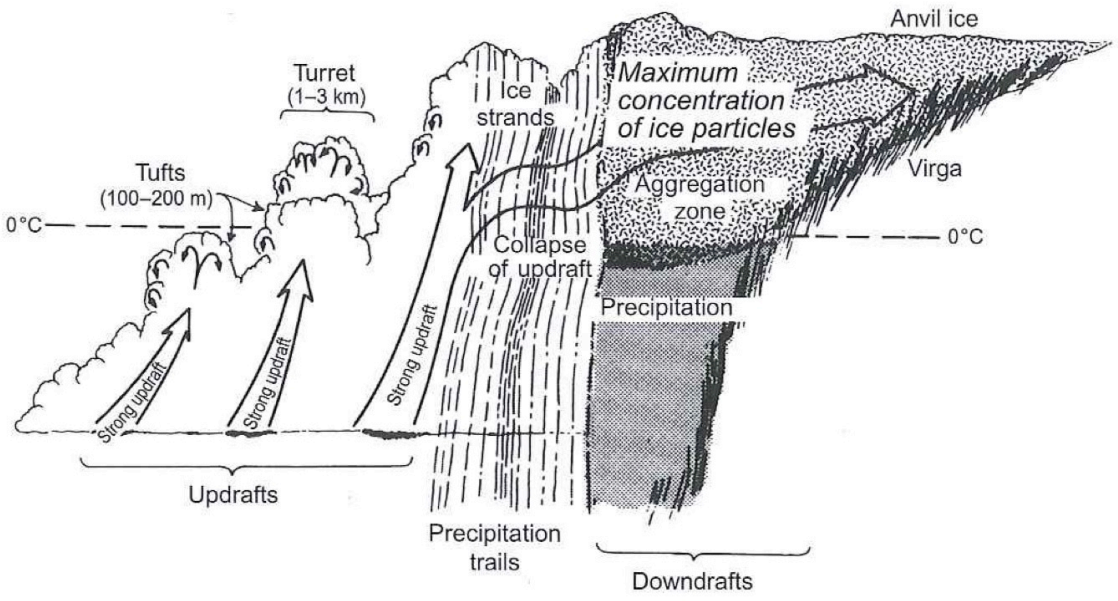

Figure 18. An idealized schematic of the lifetime of a cumulonimbus cloud and its transition from convective to stratiform stages. From Houze (2014).

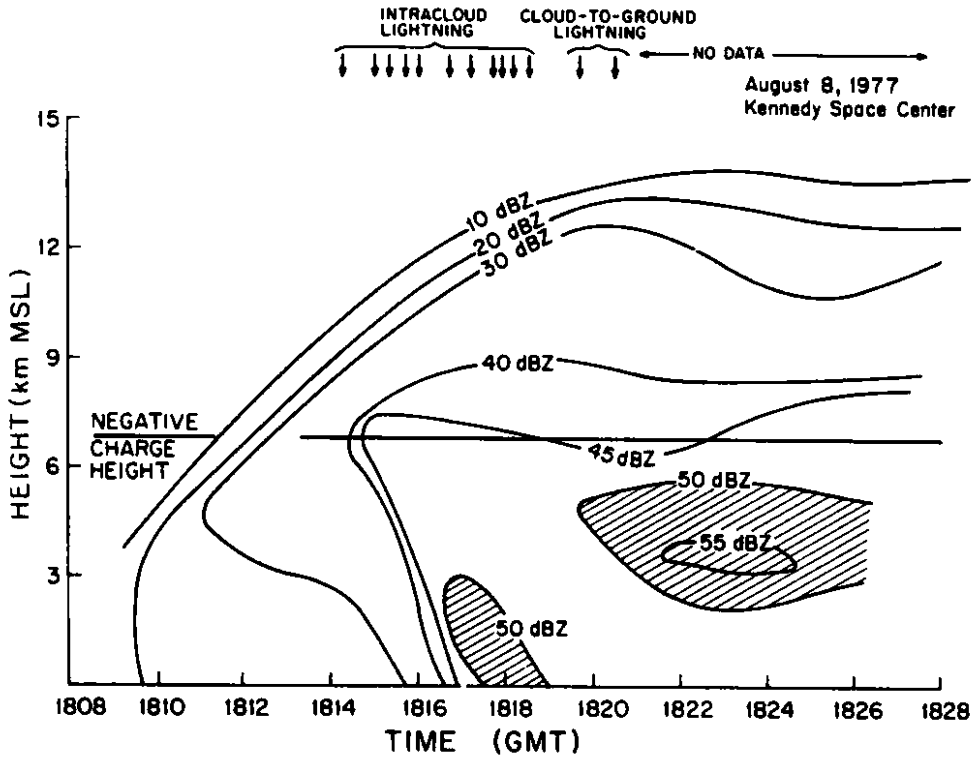

Figure 19. An idealized vertical profile of reflectivity values for the cumulonimbus transition shown in Figure 18. From Houze (2014).

Many of the changes illustrated in these schematics can be seen in the CFADs shown in Figure 20 made as the storm passed over the site. The first CFAD (Figure 20a) shows a convective profile in the updraft portion of the storm. The reflectivities are low because water is still condensing and any hydrometeors present are still growing as they are lofted up. Figure 20b shows a branch of higher reflectivity that breaks off just below 7 km and descends all the way to the surface, reaching reflectivity values above 40 dBZ. We refer to this branch as a descending arm. The descending arm represents the initial collapse of the updraft when the hydrometeors become too heavy to be supported and a

mass of rain and air descends rapidly in a convective downdraft. It is at this stage of the storm that a large quantity of ozone is brought to the surface and increases the ambient amount anywhere from 3.1 to 39.8 ppbv (in this case, the ozone enhancement was 20 ppbv). The storm then transitions to a stratiform stage (Figs, 20c and d). Reflectivity values increase with decreasing height as precipitation continues to fall and the larger, numerous hydrometeors fill the radar domain.

We postulate that CFADs are useful in identifying the approximate origin of the convective downdrafts that bring ozone to the surface since descending arms are present during a majority of the ozone enhancement events observed during the GoAmazon2014/5 campaign. Their shape and distinctiveness may also give an indication of the timing and magnitude of the enhancement events.

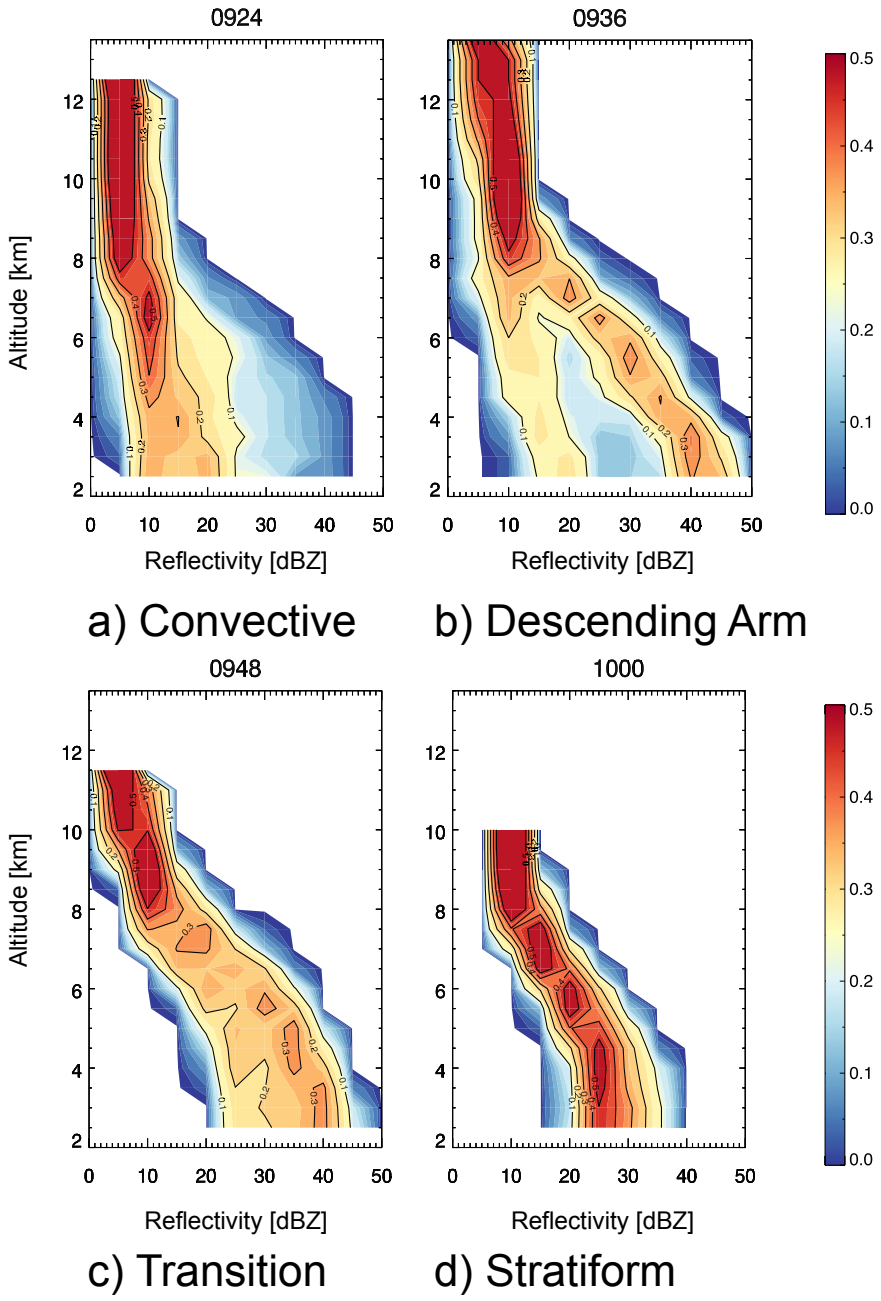

Figure 20. A case study from 19 June 2014 that shows the transition of the storm from convective to stratiform using CFADs.

3. RESULTS

3.1 Case Studies

The presence of an ozone enhancement event at the surface during strong convective events is well established, but details about the convective structure and transport during these events is not. During ozone events, the vertical structure of reflectivity values can tell us a lot about the convective transport that is taking place. I chose three case studies of varying surface ozone enhancement strengths to illustrate the strong relationship between the ozone events and the vertical profiles of reflectivity. Case #1 is representative of a low intensity case with an observed change in ozone at the surface of 4.5 ppbv. Case #2 is a medium intensity case (delta ozone = 10.2 ppbv) and Case #3 is a high intensity case (delta ozone = 22.2 ppbv). In all three cases, an enhanced branch of reflectivity that extends from 4-6 km down to the surface at the time of the maximum surface ozone is apparent, and proves to be a robust phenomenon for these ozone events.

Case #1, the low intensity case, took place on 21 December 2014 at 1948 UTC (15:48 LT). December falls toward the end of the transition from the dry to wet season. A CAPPI image from this time (Figure 21) shows isolated convective cells over T3. These cells moved slowly WSW across T3 over the course of several hours. The ozone enhancement event took place at 1948 UTC when a strong cell with reflectivity values above 45 dBZ was positioned right over the instrument site. The vertical profiler reflectivity and vertical velocities for this time show enhanced reflectivities and

descending motion (shades of blue in the bottom figure) right before the time of maximum surface ozone at 1939 UTC (indicated by the red dashed line). CFADs made for the volume scan closest to the event and representative times before and after show the evolution of the vertical structure of reflectivity during the ozone event. The profile starts off with reflectivity values concentrated at low values. The second CFAD, made for the time of maximum surface ozone, shows a descending arm that breaks off just below 8 km and descends all the way to the surface, reaching reflectivity values above 40 dBZ. The descending arm is a robust feature seen during most of the ozone enhancement events. It corresponds in time with the observed maximum surface ozone and the presence of descending motion in the vertical profiler vertical velocities. As the storm continues to move, the reflectivity values decrease in magnitude with only light rain occurring at the surface.

Case #2, the medium intensity case, took place on 8 January 2015 at 1400Z (10:00 LT). The time series of 2.5 km CAPPI images in Figure 22 shows several small, but intense cells over T3 that strengthen, merge and slowly move westward. The convection is slightly more organized over the T3 site than in the previous case. The vertical profiler shows enhanced reflectivity reaching above 8 km and a bright band right at 5 km. The vertical velocity shows some descending motion right before the time of maximum surface ozone. The first CFAD profile shows lower reflectivity values that reach up to 9 km. As the storm intensifies, a branch of enhanced reflectivity breaks away from the profile near 7 km and reaches down to the surface in the second CFAD. This descending arm is more distinct than in the previous case. The third CFAD shows the

profile move to higher reflectivity values at lower altitudes as strong rain and the associated downdrafts overtake the 22 km x 22 km grid box.

Case #3, the highest intensity ozone enhancement case, shows a similar pattern with the most defined descending arm (Figure 23). This event took place on 13 November 2014 at 0436Z (0036LT). This convection was the most organized of the three events with a leading conglomerate of strong cells and a trailing stratiform region. The strongest ozone values were observed as the first of the cells passed over T3. The vertical profiler data shows the ozone event happened just after the onset of strong reflectivity values and the strongest observed descending motion. The CFADs in this case show a very clear transition from the early convective profile, to a strong descending arm that originates above 6 km and then a transition to a stratiform profile as the stronger convection moves beyond T3 to the west.

Based on these case studies, it appears that the descending arms were sensitive to the strength of the ozone events. The stronger the ozone event, the better defined the descending arm. This is likely due to stronger convection bringing air from higher up with a larger ozone concentration. Over the course of their lifetime, strong storms can mix the troposphere, which decreases the gradient of ozone with height, but the descending arm takes place at the initiation of the downdraft and would likely happen before significant mixing takes place.

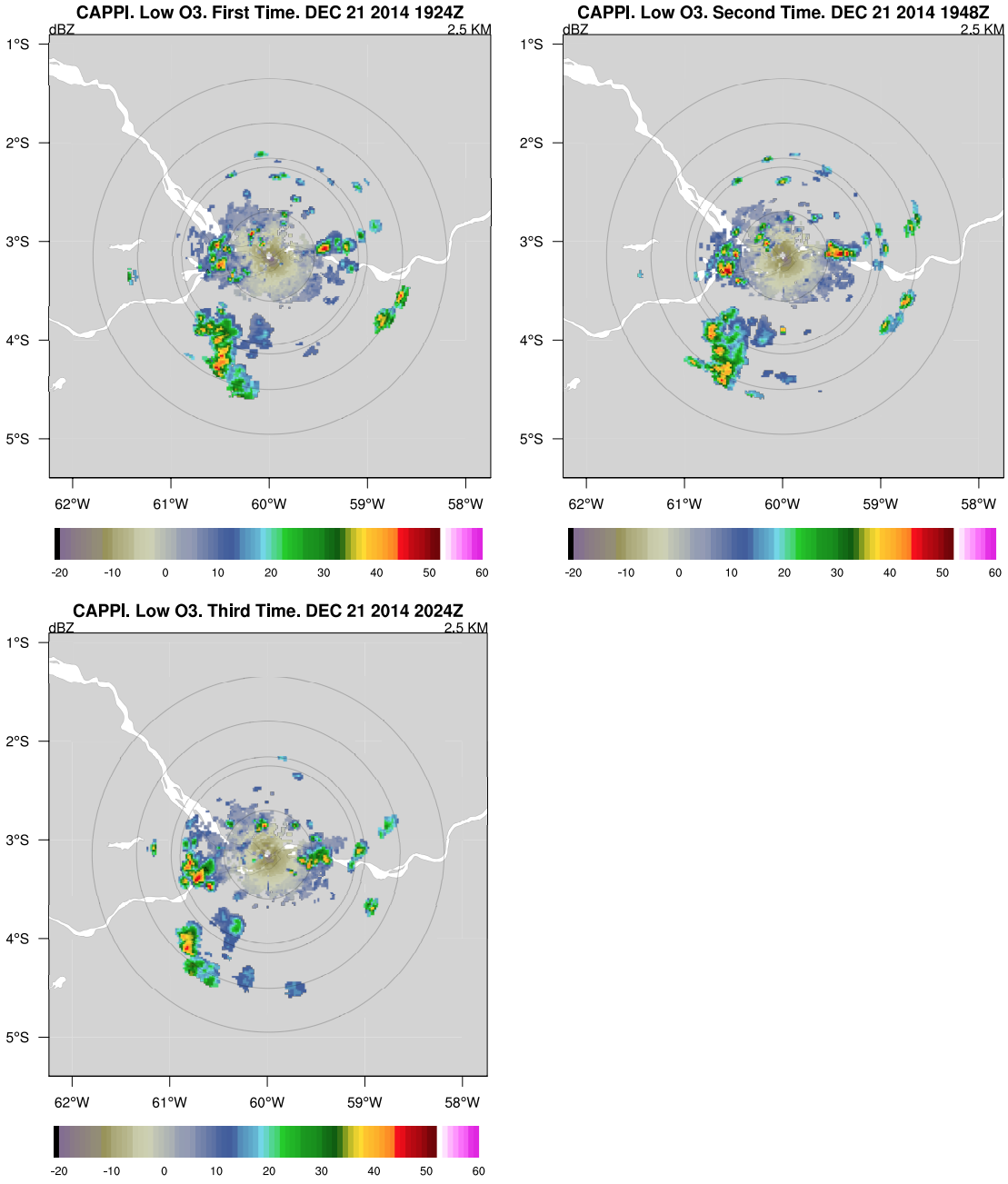

Figure 21. Case Study #1, the low intensity ozone event, took place on 21 December 2014 at 1948 UTC (15:48 LT) and increased ozone at the surface by 4.5 ppbv. The first three images are 2.5 km CAPPIs showing the evolution of the storm. The next three show CFADs made for these radar volume scans. The final image shows the reflectivity and vertical velocity profiles from the vertical profiler at T3.

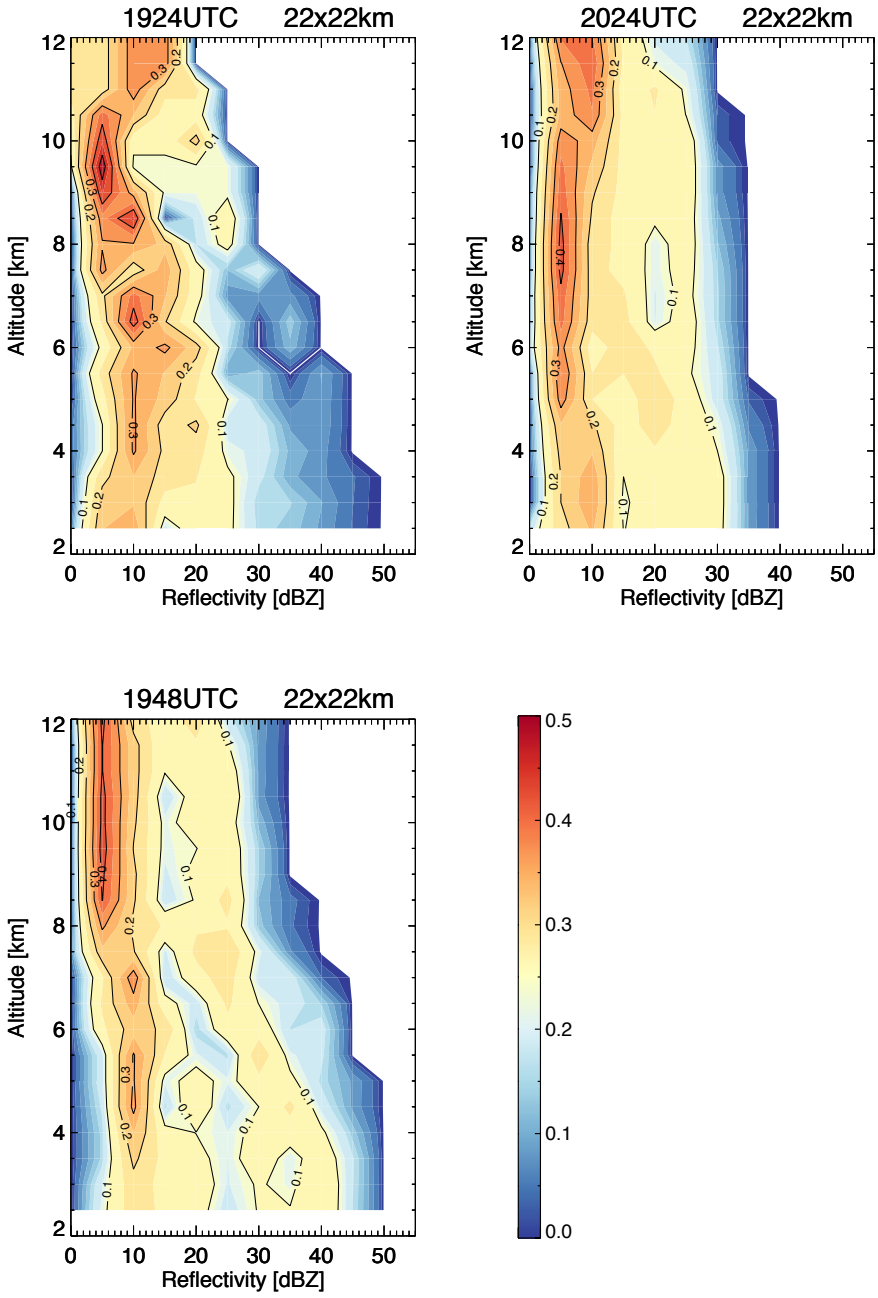

Figure 21. Continued.

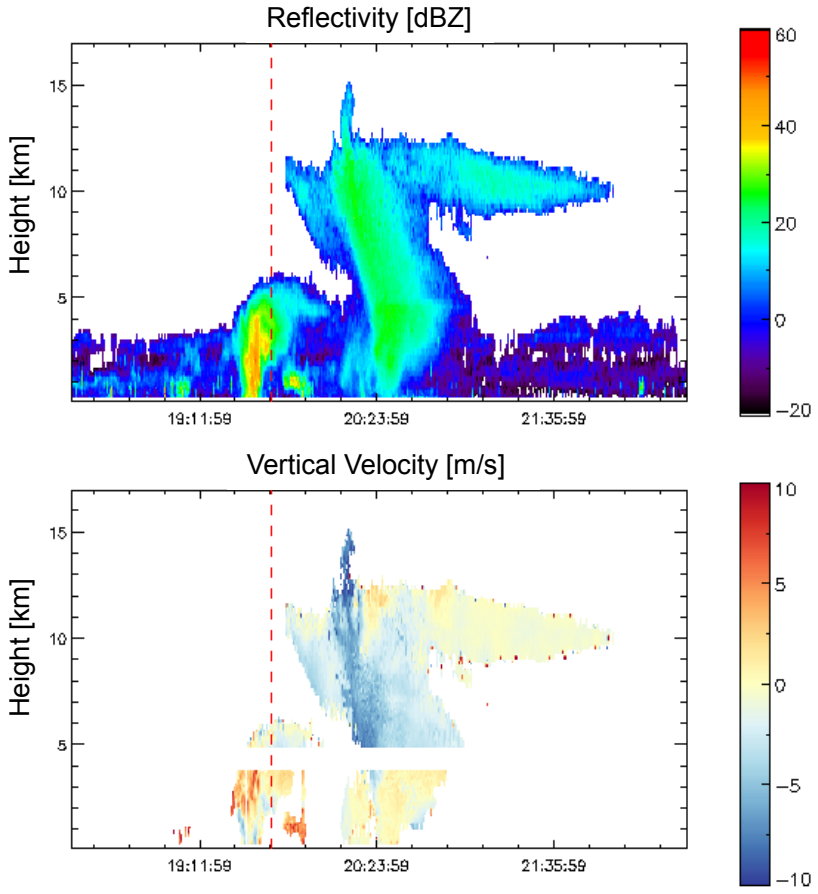

Figure 21. Continued.

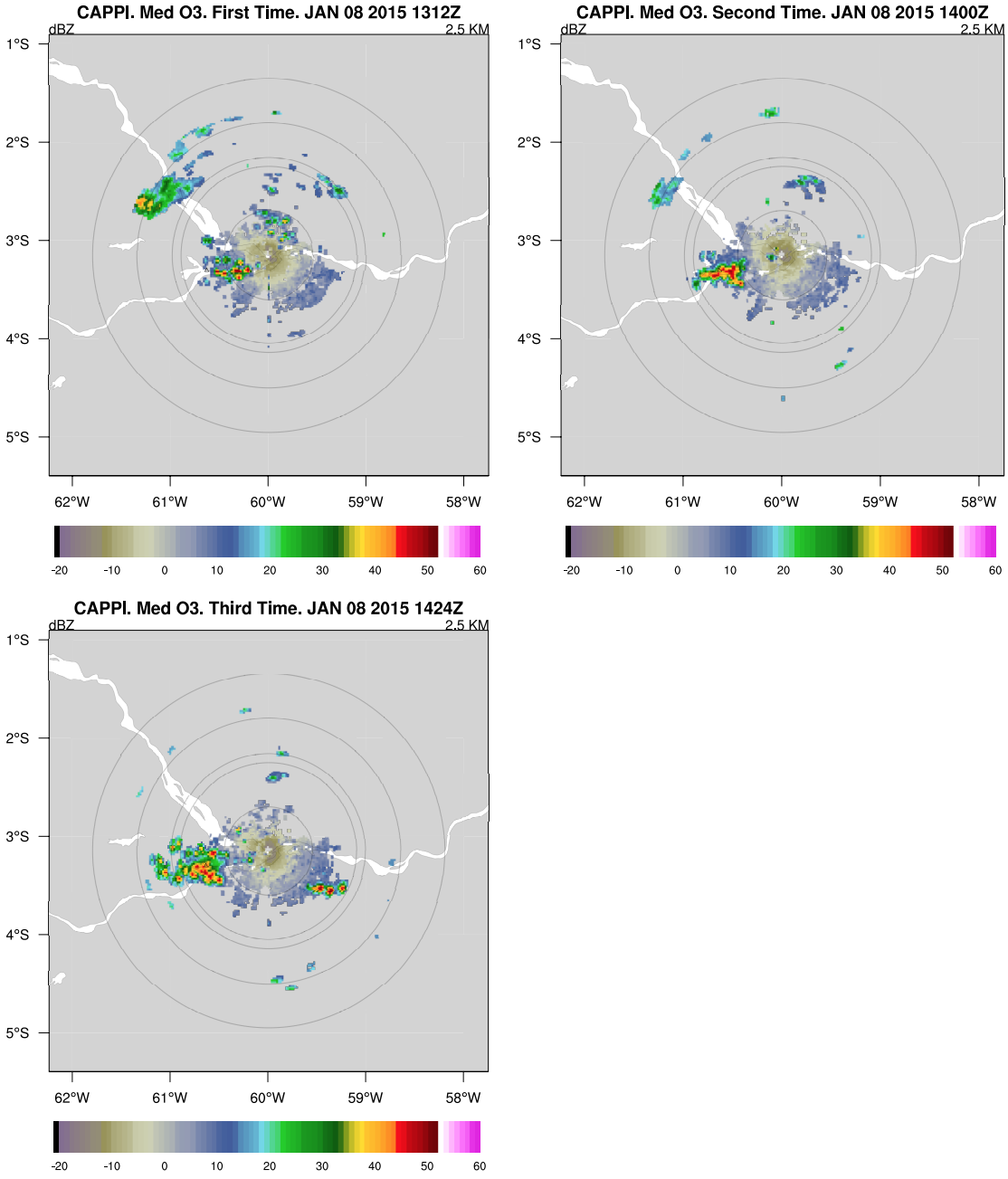

Figure 22. Case Study #2, the medium intensity ozone event, took place on 8 January 2015 at 1400Z (10:00 LT) and increased ozone at the surface by 10.2 ppbv. The remaining images are the same as shown in Figure 21 for this storm.

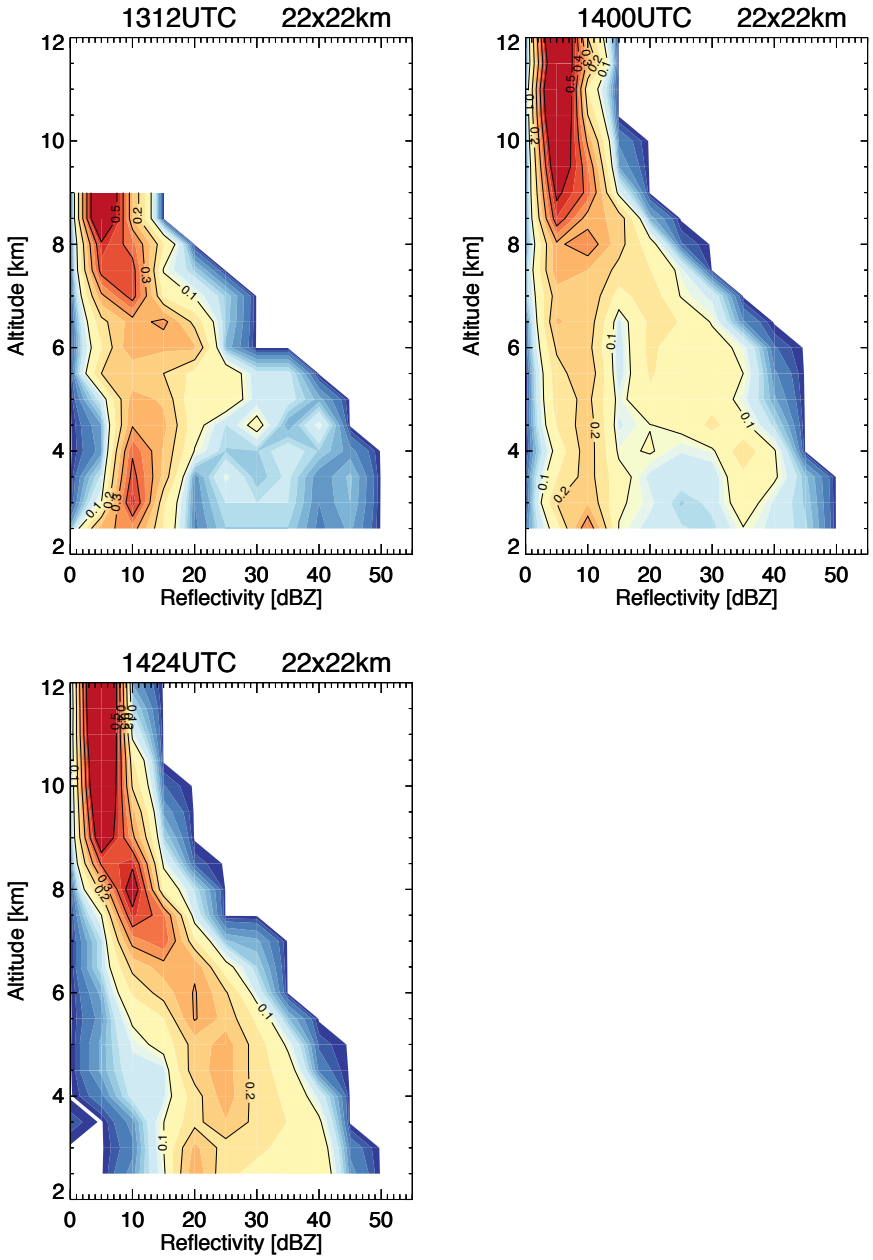

Figure 22. Continued.

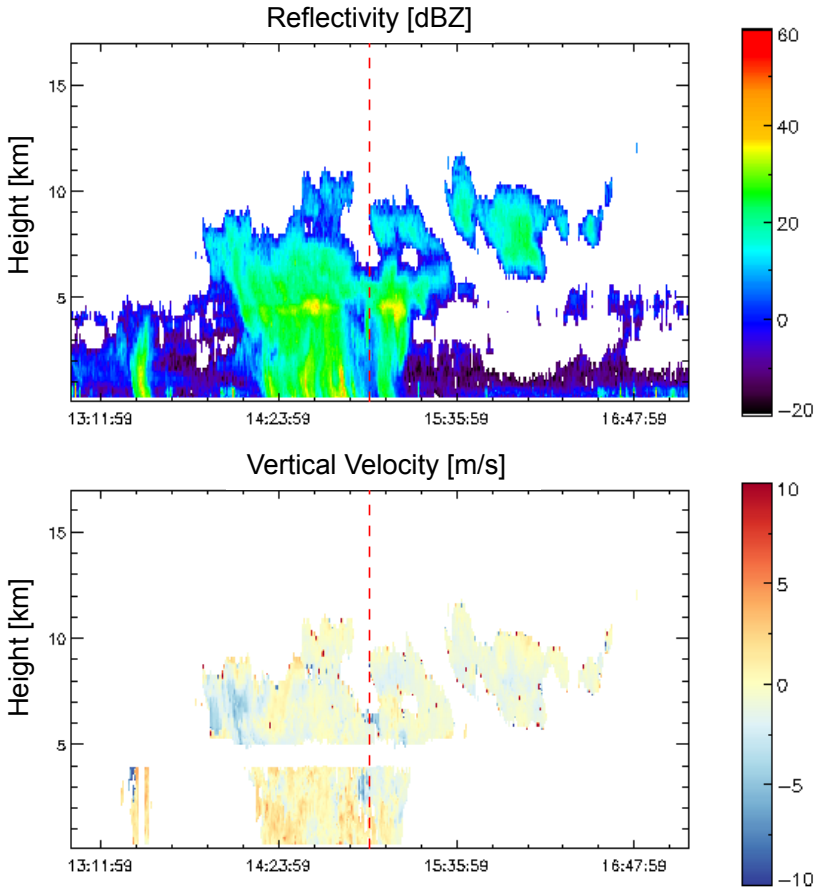

Figure 22. Continued.

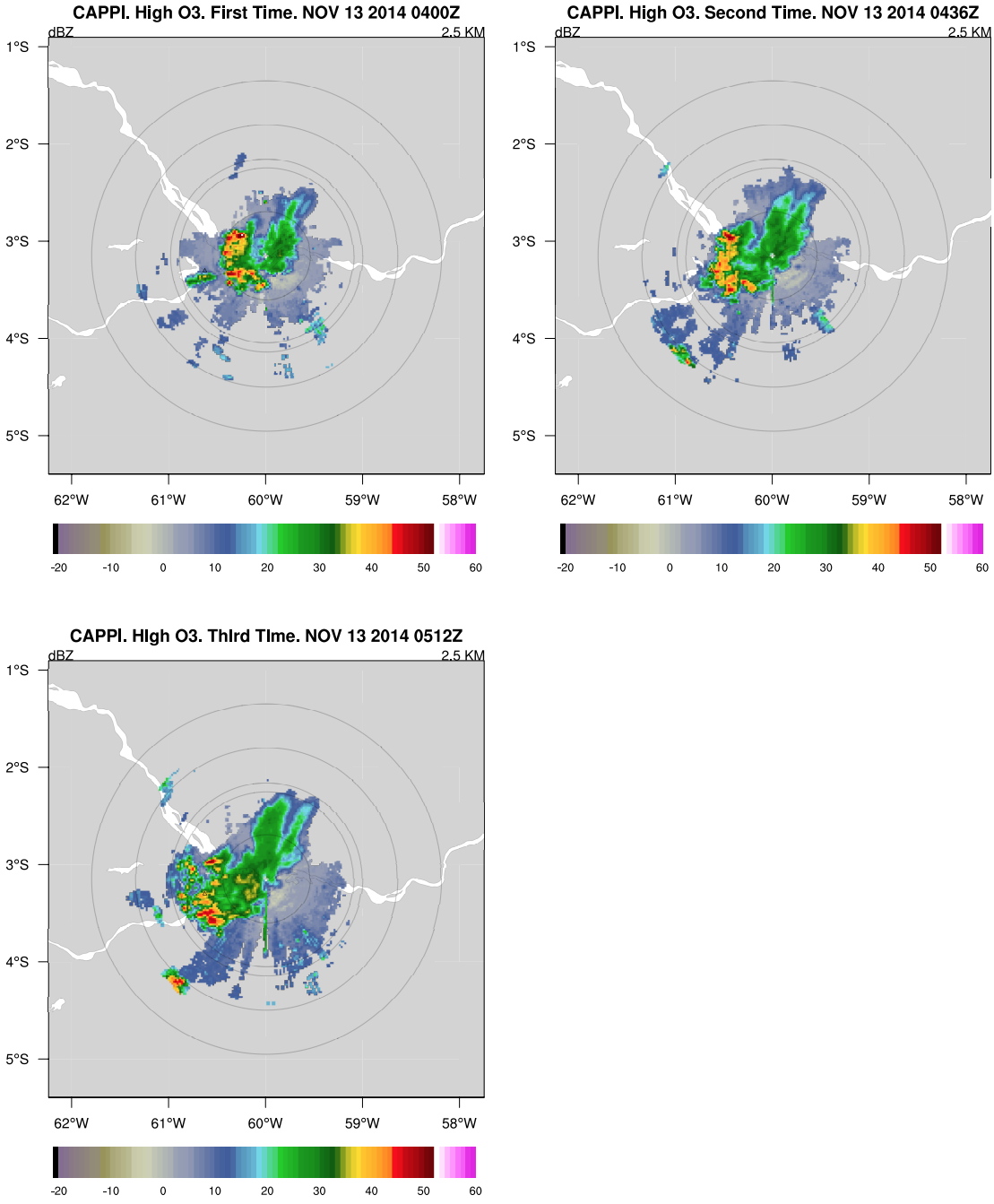

Figure 23. Case Study #3, the high intensity ozone event, took place on 13 November 2014 at 0436Z (0036LT) and increased ozone at the surface by 22.2 ppbv. The remaining images are the same as shown in Figure 21 for this storm.

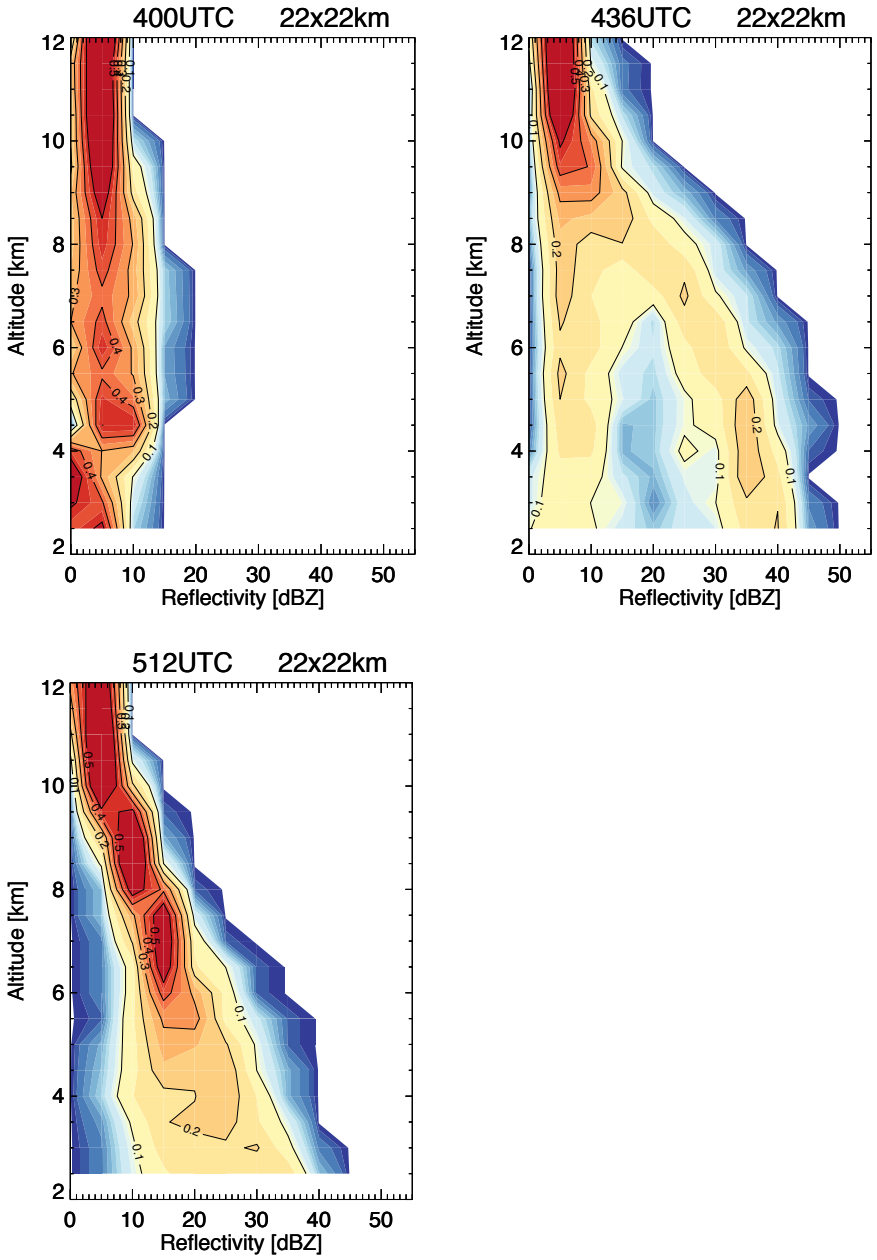

Figure 23. Continued.

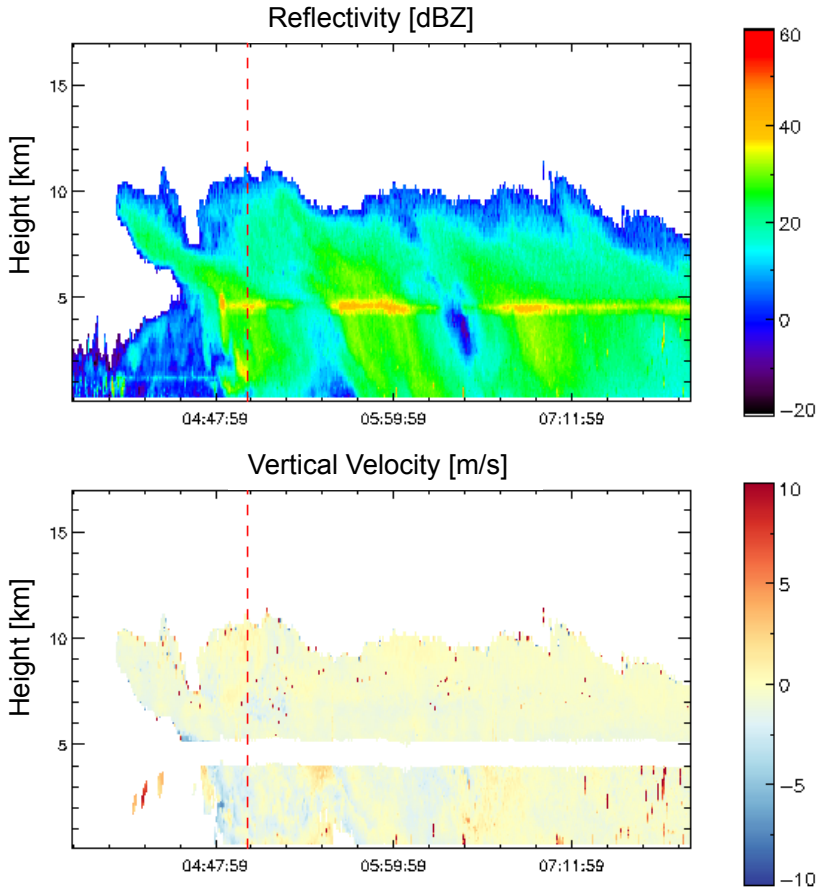

Figure 23. Continued.

3.2 CFAD Sensitivity to Spatial Scale

As mentioned in Sec. 2, CFADs are normally used to represent the entire radar domain and are often averaged over long time scales. We were limited to the innate temporal resolution of the 12-minute SIPAM volume scans. In all observed cases, the descending arm always takes place within +/- 12 minutes from the time of maximum observed surface ozone. Higher temporal resolution radar data would likely lead to more

information about the evolution and dissipation of the descending arms. However, updrafts and downdrafts can coexist on a variety of spatial scales, so I tested the sensitivity of the CFADs and the presence of descending arms to various spatial resolutions.

The ozone measurements we have available are point measurements and our focus is on what is happening within a close vicinity to the instrument site. I experimented with a range of areas between 2 x 2 km (the smallest resolution available) up to a 50 x 50 km box centered over T3. Figure 24 shows CFADs from the three case studies in Figures 11-13 made for three different sizes (i.e., 14, 22, and 44 km grids) to illustrate the effects of a changing the domain size. The smaller grid sizes were generally insufficient in capturing enough of the updraft and downdraft portions of the storm unless the convection was happening directly and exclusively within the grid box that contained T3. The larger sizes included too much surrounding convection, especially during large wet season systems, and storm details were washed out making those CFADs less useful for this purpose.

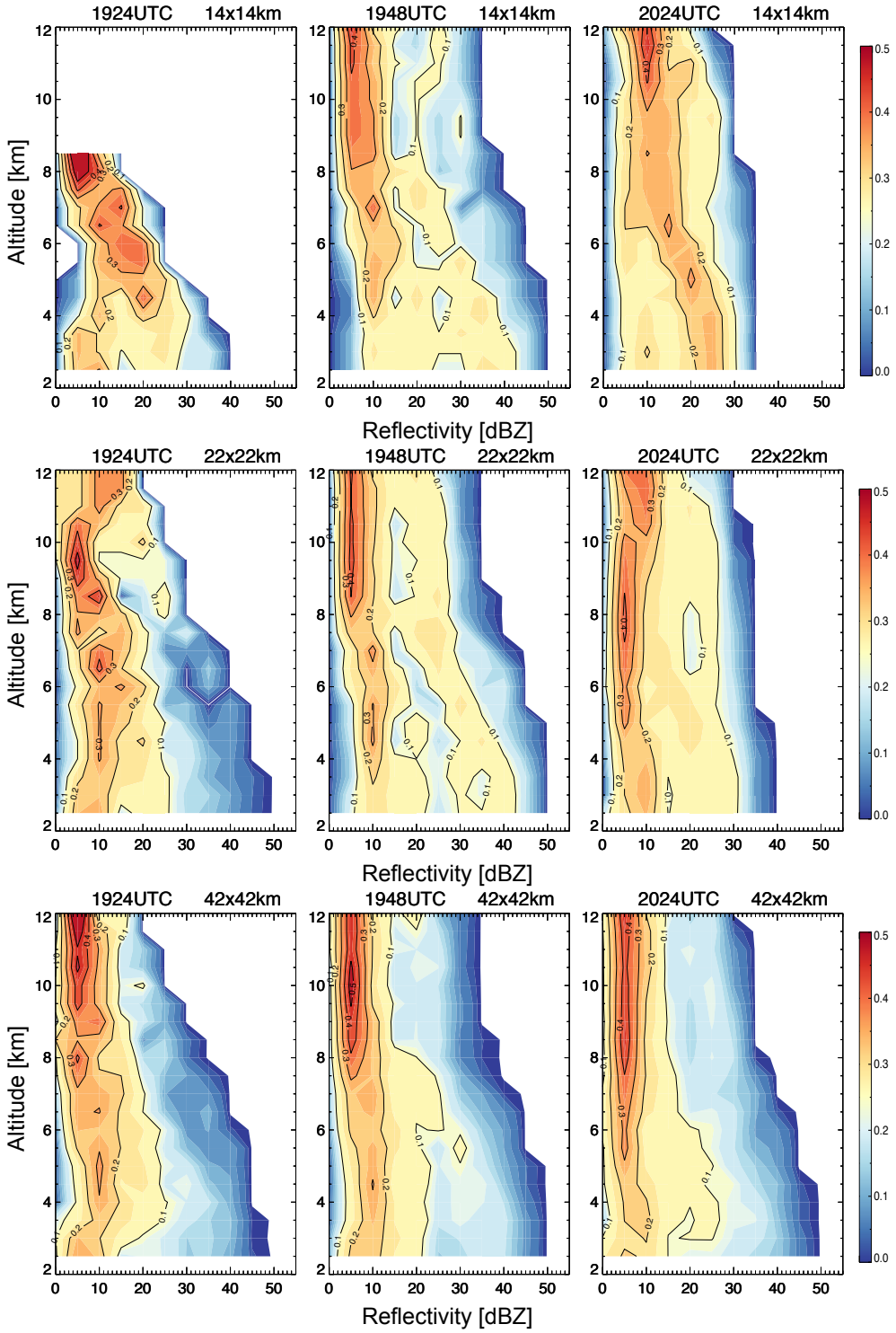

Figure 24. CFADs for the times surrounding the Case #1 ozone event made for three different domain sizes (14 x 14 km, 22 x 22 km, and 42 x 42 km) centered over T3. Time increases from left to right and the domain size increases from top to bottom. Each column represents the same time.

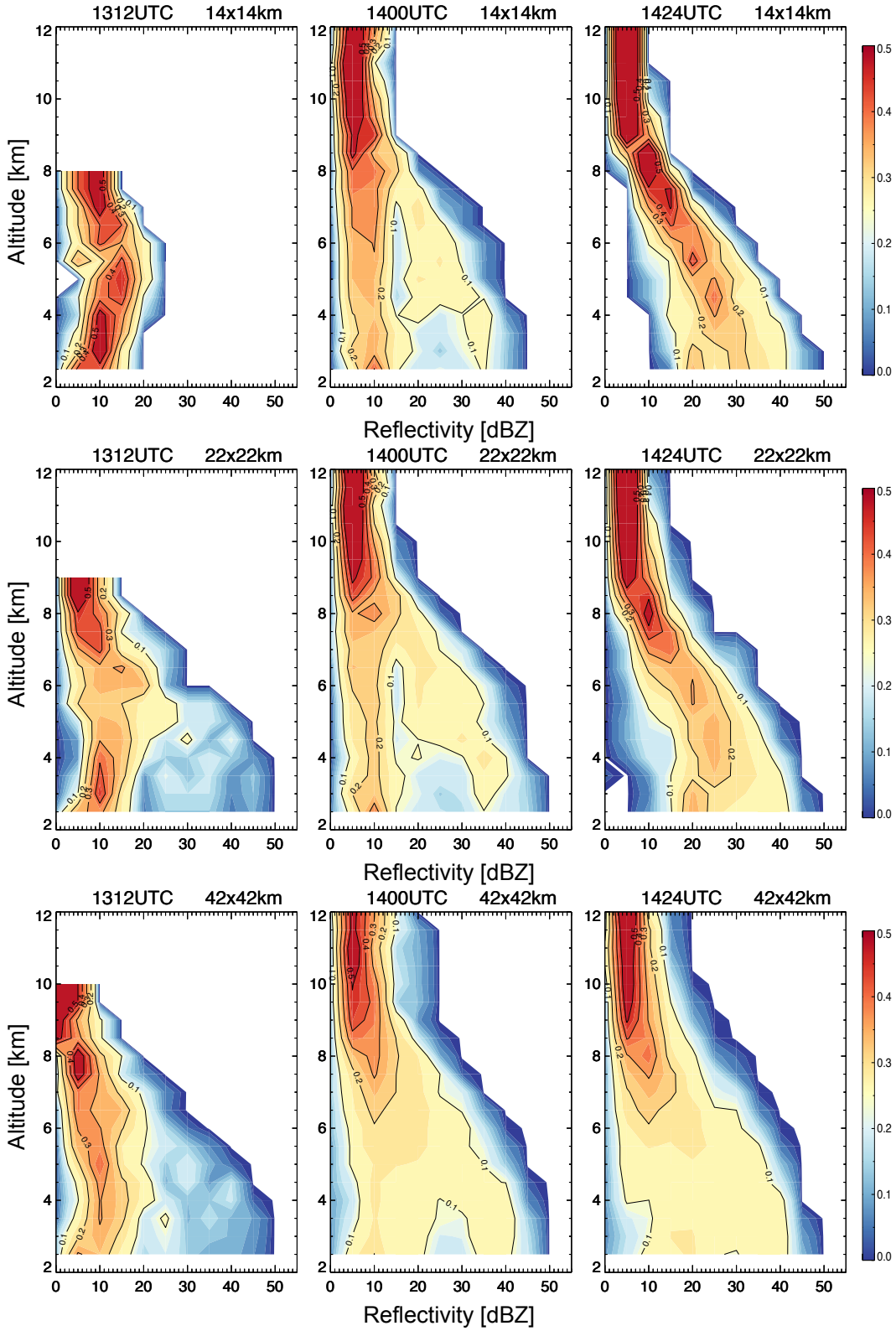

Figure 25. Same as Figure 24 but for Case #2.

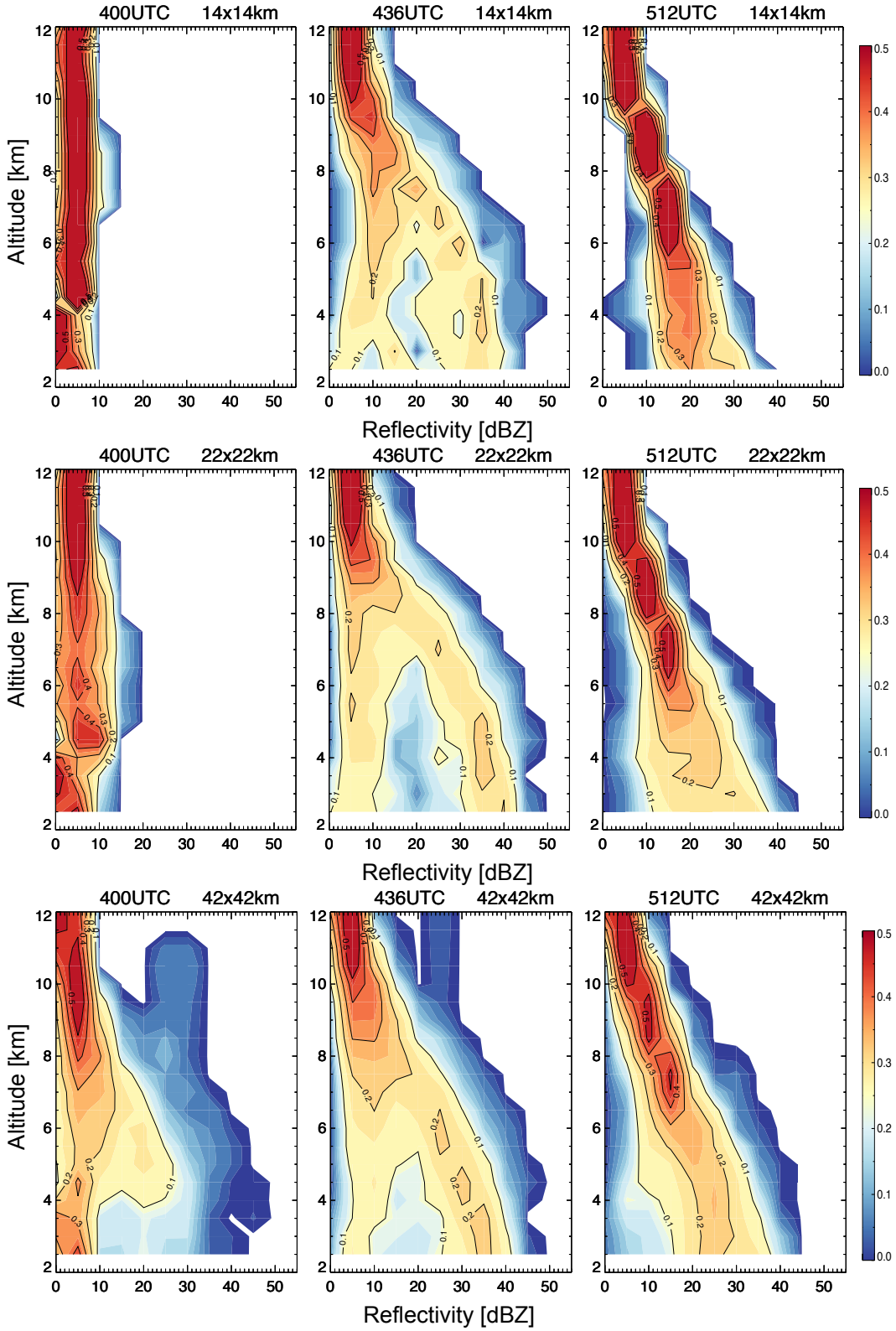

Figure 26. Same as Figure 24 but for Case #3.

A size of 22 x 22 km, which is 11 x 11 grid boxes, centered over T3 was found to be the ideal size for viewing the descending arm and storm characteristics during ozone enhancement events.

3.3 CFAD Ozone Composites

Similar to the seasonal composite CFADs in Sec. 2.5, composite CFADs were made to test the robustness of the descending arm for all observed ozone events (Figure 27). The time of maximum surface ozone was recorded for all ozone events observed at the T3 location. The radar volume scan that contained this time was considered the center and thought to be the time most likely to contain the descending arm. Two volume scans on either side of the maximum time (+/- 24 minutes) were also used to create composites. Five total composites were made to illustrate the average evolution of each storm over the course of an hour.

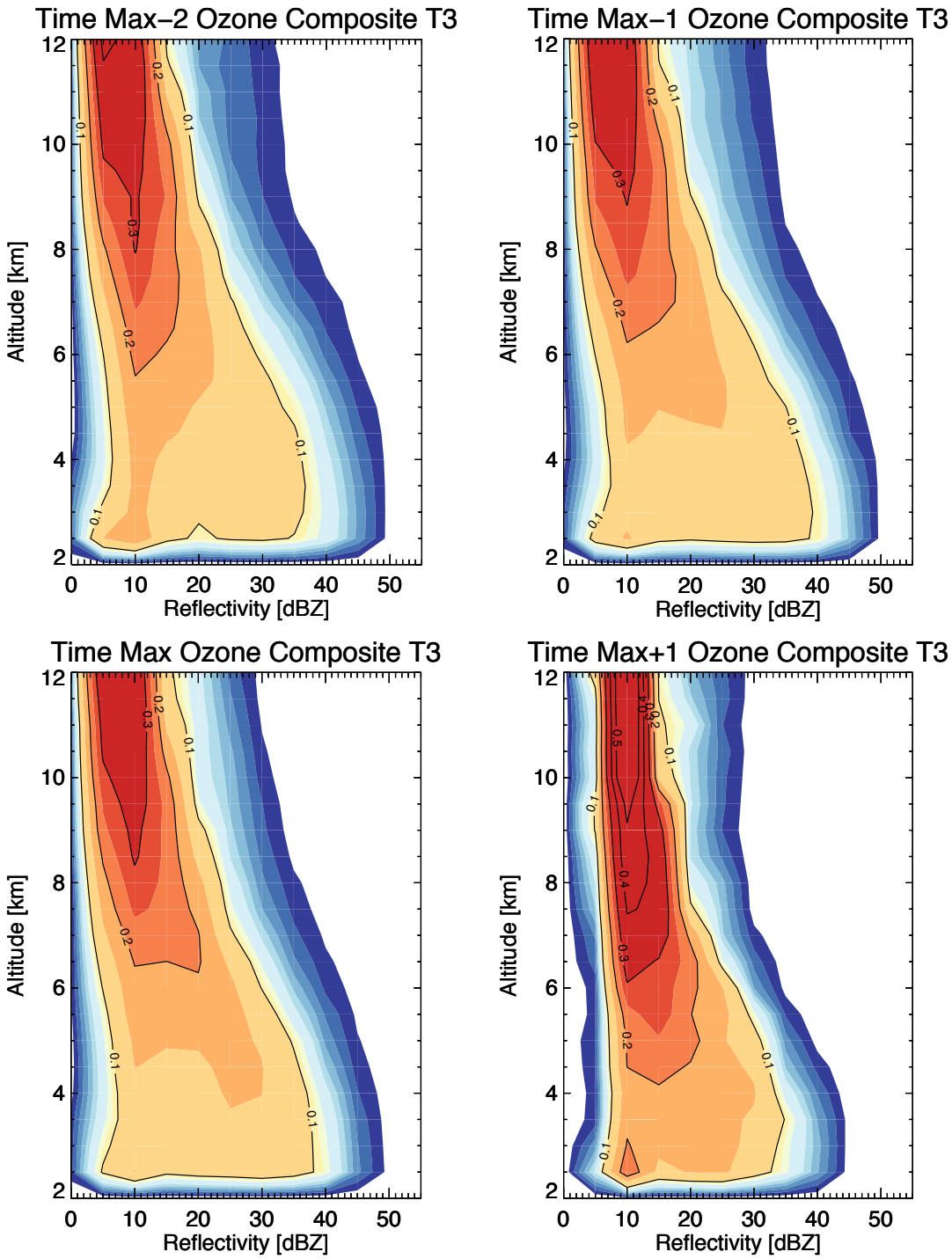

Figure 27. CFAD composites centered around the time of maximum observed surface ozone. The gap between each image is 12 minutes, so together the 5 images show the storm evolution over 1 hour.

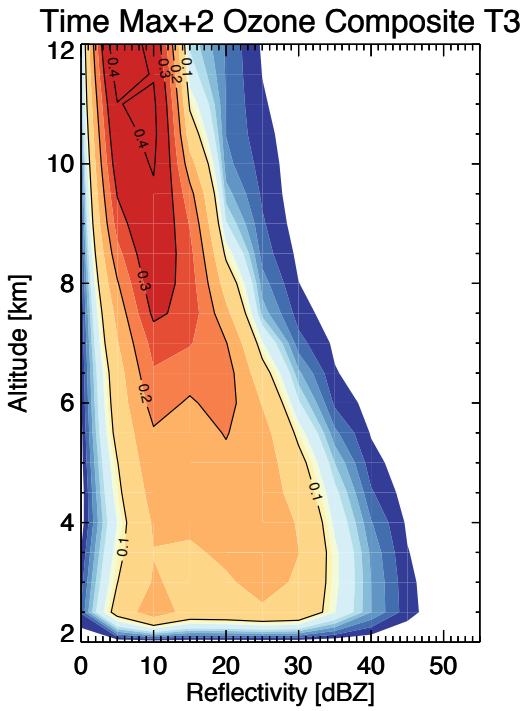

Figure 27. Continued.

While the descending arm isn't as clear as during the individual cases, there is some expansion in reflectivity noticeable near 5 km as the time approaches the time of max ozone. The time of max ozone shows a shallow descending arm of reflectivities, but it does not make it all the way to the surface. The last two composites show higher concentrations of larger reflectivity values at lower levels compared to the two previous images, but a clear transition to a stratiform type profile is not evident. The variability in storm characteristics and the wide range in strength of ozone events could have aided in washing out the details of the individual events, so we explore a more quantitative method for determining the characteristics of the descending arm.

3.4 Descending Arm Metric

The need for a concise way to describe the strength of the descending arm led to the creation of an objective method, the descending arm metric. The basic idea is to plot the frequency distributions of reflectivity at each height level individually and then determine whether there is a bimodal distribution and if so, how strongly separated the peaks are. Figure 28 shows the frequency distributions of reflectivity for all levels between 2.5 and 12.5 km at the time of max ozone from the composite CFADs in Fig. 27. At 12.5 km, the distribution has a single peak at low reflectivities. As we descend, the distribution becomes bimodal at 6.5 km, which we take as the start of the descending arm and height of the origin of the convective downdraft. The strongest separation between the bimodal distribution occurs at 4 km and represents the strength of the descending arm.

More quantitatively, the bin sizes are split in half (0-19 dBZ and 20-55 dBZ) and the maximum value is identified in each half. Then the minimum value in between these two maximum values is identified. If the minimum value is less than the second peak, the descending arm metric is calculated by subtracting the frequency of the first peak from the frequency of the second peak. If only a single peak is identified no descending arm metric is calculated.

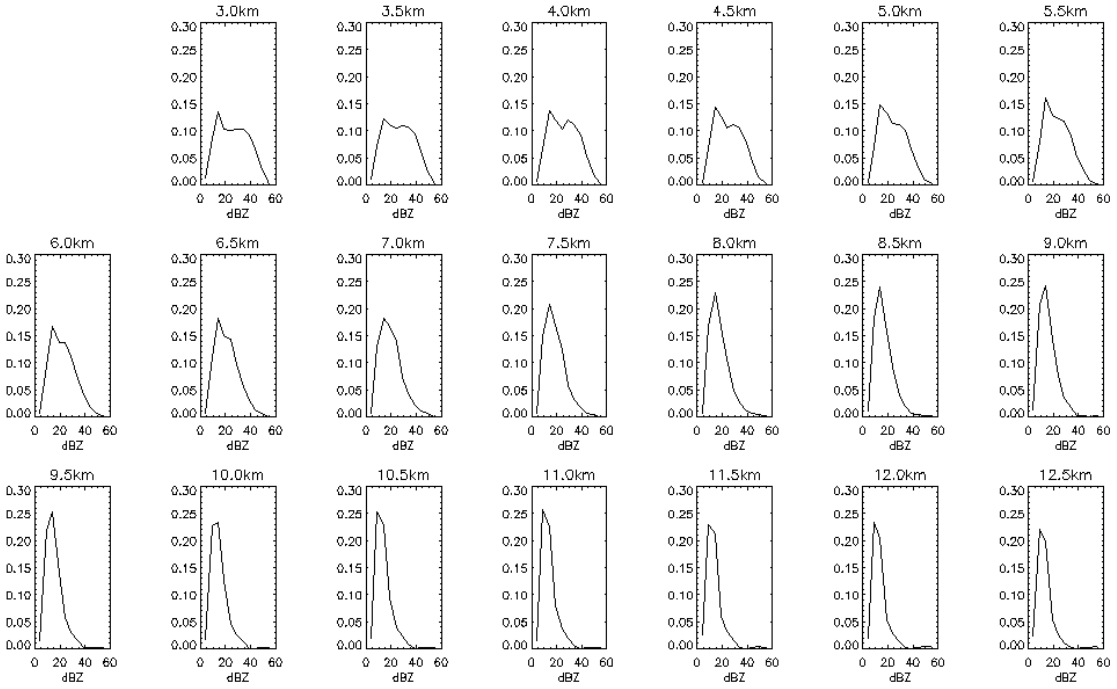

Figure 28. The composite frequency distributions for the time of max ozone at height levels 2.5 to 12 km. A bimodal peak, indicating the presence of a descending arm, is first seen at 6.5 km and is most distinct at 4 km.

Several problems arose with the automatic detection of the descending arm metric. Although rare, the method does not work when both peaks fall within the same half of the reflectivity range (e.g., both peaks are in the range from 0-19 dBZ or 20-55 dBZ). Because of the relatively small number of events, these cases were corrected by hand to get a realistic representation of the descending arm metric magnitude. Future work would include making this method more efficient to avoid such mistakes. A possible solution might include identifying peaks using a function that identifies local minima and maxima.

The magnitude of the descending arm metric represents the strength of the descending arm. A positive descending arm metric value indicates that the concentration of reflectivity values within the descending arm was higher than the remaining convective portion. A negative descending arm metric indicates a weak descending arm. Having this metric now allows us to detect descending arms and test their sensitivity to more environmental characteristics.

4. CONCLUSIONS AND FUTURE WORK

CFADs made over a smaller area have proven useful in gathering information about the structure and evolution of storms during ozone enhancement events over the Amazon. The vertical structure of reflectivity values laid out in this way can tell us a lot about the convective transport taking place. CFADs and corresponding theta-e measurements are useful in identifying the approximate origin of the convective downdrafts that bring ozone to the surface. The shape and distinctiveness of the CFADs also gives an indication of the timing and magnitude of the enhancement events. The vertical profilers present during the campaign confirmed the presence of descending motion.

The descending arm, a CFAD feature characteristic of descending motion, proved to be a robust feature during a majority of the ozone enhancement events observed during the GoAmazon2014/5 campaign. Composite images of CFADs showed the descending arm takes place in close proximity to the time of maximum observed surface ozone. The descending arm feature of these CFADs provides an accessible way to track the convective transport of trace gases such as ozone. This methodology could be expanded over an entire radar domain where surface ozone measurements are not available to predict ozone enhancement events in the presence of convection.

The descending arm metric is a simple tool useful for identifying and quantifying the relative strength of descending arms. The descending arm metric takes advantage of the difference in reflectivity frequencies between the two peaks in the presence of a

descending arm. In a distribution with a single peak there is no descending arm and thus less variability in storm vertical motion over the horizontal scale of a few convective cells. This metric can be used to compare the strengths of descending arms to various environmental factors. Future work will further explore and refine the use of automated techniques for identifying and categorizing descending arms and their use in identifying the presence and strength of convective cold pools.

REFERENCES

Bertram, T. H., A. E. Perring, P. J. Wooldridge, J. D. Crounse, A. J. Kwan, P. O. Wennberg, E. Scheuer, J. Dibb, M. Avery, G. Sachse, S. A. Vay, J. H. Crawford, C. S. McNaughton, A. Clarke, K. E. Pickering, H. Fuelberg, G. Huey, D. R. Blake, H. B. Singh, S. R. Hall, R. E. Shetter, A. Fried, B. G. Heikes, and R. C. Cohen, 2007: Direct Measurement of the Convective Recycling of the Upper Troposphere. *Science,* **315**, 816–820.

Betts, A. K., 1973: A Composite Cumulonimbus Budget. *Journal of the Atmospheric Sciences*, **30**, 597–610.

Betts, A. K., 1992: FIFE Atmospheric Boundary Layer Budget Methods. *Journal of Geophysical Research*, **97**, 18523–18532.

Betts, A. K., L. V. Gatti, A. M. Cordova, M. A. F. Silva Dias, and J. D. Fuentes, 2002: Transport of Ozone to the Surface by Convective Downdrafts at Night. *Journal of Geophysical Research*, **107**, 8046.

Betts, A. K., M. A. F. Silva Dias, 1979: Unsaturated Downdraft Thermodynamics in Cumulonimbus. *Journal of the Atmospheric Sciences*, **36**, 1061–1071.

Chatfield, R. B., and P. J. Crutzen, 1984: Sulfur Dioxide in Remote Oceanic Air: Cloud Transport of Reactive Precursors. *Journal of Geophysical Research*, **89**, 7111–7132.

Dickerson, R. R., G. J. Huffman, W. T. Luke, L. J. Nunnenmacker, K. E. Pickering, A. C. D. Leslie, C. G. Lindsey, W. G. N. Slinn, T. J. Kelly, P. H. Daum, A. C. Delany, J. P. Greenberg, P. R. Zimmerman, J. F. Boatman, J. D. Ray, and D. H. Stedman, 1987: Thunderstorms: An Important Mechanism in the Transport of Air Pollutants. *Science*, **235**, 460–465.

Emanuel, K. A., 1994: Atmospheric Convection. *Oxford University Press,* 580 pp.

Garstang, M., J. Scala, S. Greco, R. Harriss, S. Beck, E. Browell, G. Sachse, G. Gregory, G Hill, J. Simpson, W. Tao, and A. Torres, 1988: Trace Gas Exchanges and Convective Transports Over the Amazonian Rain Forest. *Journal of Geophysical Research*, **93**, 1528–1550.

Gerken, T., D. Wei, R. J. Chase, J. D. Fuentes, C. Schumacher, L. A. T. Machado, R. V. Andreoli, M. Chamecki, R. A. Ferreira de Souza, L. S. Freire, A. B. Jardine, A. O. Manzi, R. M. Nascimento dos Santos, C. von Randow, P. d. S. Costa, P. C. Stoy, J. Tóta, and A. M. Trowbridge, 2015: Downward Transport of Ozone Rich Air and Implications for Atmospheric Chemistry in the Amazon Rainforest. *Atmospheric Environment*, **124,** 64–76.

Giangrande, S. E, S. Collis, J. Straka, A. Protat, C. Williams, and S. Krueger, 2013: A Summary of Convective-Core Vertical Velocity Properties Using ARM UHF Wind Profilers in Oklahoma. *Journal of Applied Meteorology and Climatology*, **52**, 2278–2295.

Gidel, L. T., 1983: Cumulus Cloud Transport of Transient Tracers. *Journal of Geophysical Research*, **88**, 6587–6599.

Grant, D. D., J. D. Fuentes, M. S. DeLonge, S. Chan, E. Joseph, P. A. Kucera, S. A. Ndiaye, and A. T. Gaye, 2008: Ozone Transport by Mesoscale Convective Storms in Western Senegal. *Atmospheric Environment*, **42**, 7104–7114.

Greenhut, G. K., 1986: Transport of Ozone Between Boundary Layer and Cloud Layer by Cumulus Clouds. *Journal of Geophysical Research*, **91**, 8613–8622.

Houze, R. A., 2014: Cloud Dynamics. *Academic Press*, 432 pp.

Kirchhoff, V. W. J. H., I. M. O. Da Silva, and E. V. Browell, 1990: Ozone Measurements in Amazonia: Dry Season Versus Wet Season. *Journal of Geophysical Research*, **95**, 16,913–16,926.

Kirchhoff, V. W. J. H., J. R. Alves, F. R. Silva, and J. Fishman, 1996: Observations of Ozone Concentrations in the Brazilian Cerrado During the TRACE-A Field Expedition. *Journal of Geophysical Research*, **101**, 24,029–24,042.

Lelieveld, J. and P. J. Crutzen, 1994: Role of Deep Cloud Convection in the Ozone Budget of the Troposphere. *Science*, **264**, 1759–1761.

Machado, L. A. T., H. Laurent, N. Dessay, and I. Miranda, 2004: Seasonal and Diurnal Variability of Convection Over the Amazonia: A Comparison of Different Vegetation Types and Large Scale Forcing. *Theoretical and Applied Climatology,* **78**, 61–77.

Marks, D. A, D. B. Wolff, D. S. Silberstein, A. Tokay, J. L. Pippitt, and J. Wang, 2009: Availability of High-Quality TRMM Ground Validation Data from Kwajalein, RMI: A Practical Application of the Relative Calibration Adjustment Technique. *Journal of Atmospheric and Oceanic Technology,* **26**, 413–429.

Marshall, J. S., and W. M. Palmer, 1948: The Distribution of Raindrops with Size. *Journal of the Meteorology*, **5**, 165–166.

Pickering, K. E., A. M. Thompson, Y. Wang, W. Tao, D. P. McNamara, V. W. J. H. Kirchoff, B. G. Heikes, G. W. Sachse, J. D. Bradshaw, G. L. Gregory, and D. R. Blake, 1996: Convective Transport of Biomass Burning Emissions over Brazil During TRACE-A. *Journal of Geophysical Research*, **101**, 23993–24012.

Sahu, L. K., and S. Lal, 2006: Changes in Surface Ozone Levels due to Convective Downdrafts over the Bay of Bengal. *Geophysical Research Letters*, **33**, L10807.

Scala, J. R., M. Garstang, W. -K. Tao, K. E. Pickering, A. M. Thompson, J. Simpson, V. W. J. H. Kirchoff, E. V. Browell, G. W. Sachse, A. L. Torress, G. L. Gregory, R. A. Rasmussen, and M. A. K. Khalil, 1990: Cloud Draft Structure and Trace Gas Transport. *Journal of Geophysical Research*, **95**, 17,015–17,030.

Silberstein, D. A., D. B. Wolff, D. A. Marks, D. Atlas, and J. L. Pippitt, 2008: Ground Clutter as a Monitor of Radar Stability at Kwajalein, RMI. *Journal of Atmospheric and Oceanic Technology*, **25**, 2037–2045.

Thompson, A. M., W. -K. Tao, K. E. Pickering, J. R. Scala, and J. Simpson, 1997: Tropical Deep Convection and Ozone Formation. *Bulletin of the American Meteorological Society*, **78**,1043–1054.

Wallace, J. M., and P. V. Hobbs, 2006: Atmospheric Science An Introductory Survey. *Academic Press*, pp 483.

Yuter, S. E., and R. A. Houze, 1995: Three-Dimensional Kinematic and Microphysical Evolution of Florida Cumulonimbus. Part II: Frequency Distribution of Vertical Velocity, Reflectivity, and Differential Reflectivity. *Monthly Weather Review,* **123,** 1941–1963.

Zipser, E. J., 1969: The Role of Organized Unsaturated Convective Downdrafts in the Structure and Rapid Decay of an Equatorial Disturbance. *Journal of Applied Meteorology*, **8**, 799–814.

Zipser, E. J., 1977: Mesoscale and Convective–Scale Downdrafts as Distinct Components of Squall-Line Structure. *Monthly Weather Review,* **105**, 1568–1589.